

The Propagation, Evolution, and Rotation in Linear Storms (PERiLS) Project

Karen A. Kosiba,^a Anthony W. Lyza,^{b,c} Robert J. Trapp,^d Erik N. Rasmussen,^c Matthew Parker,^e Michael I. Biggerstaff,^f Stephen W. Nesbitt,^d Christopher C. Weiss,^g Joshua Wurman,^a Kevin R. Knupp,^h Brice Coffey,^e Vanna C. Chmielewski,^c Daniel T. Dawson,ⁱ Eric Bruning,^g Tyler M. Bell,^{b,c} Michael C. Coniglio,^{c,f} Todd A. Murphy,^j Michael French,^k Leanne Blind-Doskocil,^l Anthony E. Reinhart,^c Edward Wolff,^d Morgan E. Schneider,^{f,b,c} Miranda Silcott,^b Elizabeth Smith,^c Joshua Aikins,^a Melissa Wagner,^{b,c} Paul Robinson,^a James M. Wilczak,^m Trevor White,^a Madeline R. Diedrichsen,^{b,c,f} David Bodine,^{f,n} Matthew R. Kumjian,^o Sean M. Waugh,^c A. Addison Alford,^{c,b} Kim Elmore,^{b,c} Pavlos Kollias,^k and David D. Turner^p

KEYWORDS:

Severe storms;
Squall lines;
Tornadoes;
Mesoscale processes;
Storm environments;
Mesoscale forecasting

ABSTRACT: Quasi-linear convective systems (QLCSs) are responsible for approximately a quarter of all tornado events in the United States, but no field campaigns have focused specifically on collecting data to understand QLCS tornadogenesis. The Propagation, Evolution, and Rotation in Linear Storms (PERiLS) project was the first observational study of tornadoes associated with QLCSs ever undertaken. Participants were drawn from more than 10 universities, laboratories, and institutes, with over 100 students participating in field activities. The PERiLS field phases spanned 2 years, late winters and early springs of 2022 and 2023, to increase the probability of intercepting significant tornadic QLCS events in a range of large-scale and local environments. The field phases of PERiLS collected data in nine tornadic and nontornadic QLCSs with unprecedented detail and diversity of measurements. The design and execution of the PERiLS field phase and preliminary data and ongoing analyses are shown.

DOI: 10.1175/BAMS-D-22-0064.1

Corresponding author: Karen A. Kosiba, kakosiba@uah.edu

Supplemental information related to this paper is available at the Journals Online website:

<https://doi.org/10.1175/BAMS-D-22-0064.s1>.

Manuscript received 29 March 2022, in final form 29 May 2024, accepted 7 June 2024

© 2024 American Meteorological Society. This published article is licensed under the terms of the default AMS reuse license. For information regarding reuse of this content and general copyright information, consult the AMS Copyright Policy (www.ametsoc.org/PUBSReuseLicenses).

AFFILIATIONS: ^a Flexible Array of Radars and Mesonets, Department of Atmospheric Sciences, University of Illinois Urbana–Champaign, Urbana, Illinois; ^b Cooperative Institute for Severe and High Impact Weather Research and Operations, University of Oklahoma, Norman, Oklahoma; ^c NOAA/OAR/National Severe Storms Laboratory, Norman, Oklahoma; ^d Department of Atmospheric Sciences, University of Illinois Urbana–Champaign, Urbana, Illinois; ^e Department of Marine, Earth, and Atmospheric Sciences, North Carolina State University, Raleigh, North Carolina; ^f School of Meteorology, University of Oklahoma, Norman, Oklahoma; ^g Department of Geosciences, Texas Tech University, Lubbock, Texas; ^h Department of Earth and Atmospheric Sciences, University of Alabama in Huntsville, Huntsville, Alabama; ⁱ Department of Earth, Atmospheric, and Planetary Sciences, Purdue University, West Lafayette, Indiana; ^j Atmospheric Science, University of Louisiana at Monroe, Monroe, Louisiana; ^k The School of Marine and Atmospheric Sciences, Stony Brook University, State University of New York, Stony Brook, New York; ^l Department of Geography and Meteorology, Valparaiso University, Valparaiso, Indiana; ^m NOAA/Physical Sciences Laboratory, Boulder, Colorado; ⁿ Advanced Radar Research Center, University of Oklahoma, Norman, Oklahoma; ^o Department of Meteorology and Atmospheric Sciences, The Pennsylvania State University, University Park, Pennsylvania; ^p NOAA/Global Systems Laboratory, Boulder, Colorado

1. Introduction

Over the past 10 years, ~1400 tornadoes occurred annually in the United States, of which roughly 15%–25% are spawned by quasi-linear convective systems (QLCSs) (e.g., Trapp et al. 2005; Smith et al. 2012; Ashley et al. 2019). This percentage is even higher in the southeastern (SE) United States (Anderson-Frey and Brooks 2019), where the population is particularly vulnerable to tornado impacts (Ashley et al. 2008; Strader and Ashley 2018). Complicating the prediction of QLCS tornadogenesis is identifying when and where along the QLCS tornadoes will occur (e.g., Ashley et al. 2019; Lovell and Parker 2022). In response, considerable operational attention has been given to the “three-ingredients method” (Schaumann and Przybylinski 2012) to locally access QLCS mesovortexgenesis and, correspondingly, tornadogenesis potential, but there is uncertainty in thresholds, broad applicability, and the optimal combination of parameters (e.g., Gibbs 2021; Ungar and Coniglio 2023).

While a multitude of field campaigns have focused on collecting data to better understand supercell tornadogenesis [e.g., VORTEX (Rasmussen et al. 1994), VORTEX-2 (Wurman et al. 2012), Analysis of the Near-Surface Wind and Environment along the Rear Flank of Supercells (ANSWERS) (Lee et al. 2004), Radar Observation of Thunderstorms and Tornadoes Experiment (ROTATE) (Wurman 1998, 2003, 2008), Tornado Winds from In situ and Radars at Low level (TWIRL) (Kosiba and Wurman 2016), Rivers of Vorticity in Supercells (RiVorS) (Mahalik et al. 2018), Targeted Observation by Radars and Unmanned Aerial Systems (UAS) of Supercells (TORUS) (Houston et al. 2019), and Boundary-layer Evolution and Structure of Tornadoes (BEST) (Wurman and Kosiba 2023a)], none have focused specifically on QLCS tornadogenesis. Other field projects such as BAMEX (Davis et al. 2004), Plains Elevated Convection at Night (PECAN) (Geerts et al. 2017), and Remote Sensing of Electrification, Lightning, and Mesoscale/Microscale Processes with Adaptive Ground Observations (RELAMPAGO) (Nesbitt et al. 2021) focused on mesoscale convective systems, including QLCSs, but these projects were not primarily focused on tornado-producing systems. Gaps in our knowledge have critically reduced our ability to warn the public because common forecast skill metrics (e.g., warning lead time and false alarm rate) are significantly worse in QLCS tornado events than in supercell tornado events (e.g., Brotzge et al. 2013).

In 2016, a National Oceanic and Atmospheric Administration (NOAA)-funded project, VORTEX-SE (VSE), was conceived to improve the understanding of tornadogenesis mechanisms in the SE United States (Koch and Rasmussen 2016). The ongoing VSE project has focused on various aspects of tornadogenesis in greater northern Alabama and in Mississippi. During three spring VSE field campaigns (2016, 2017, and 2018), QLCSs were the primary storm mode associated with tornadogenesis in the study area. These campaigns provided a proof of concept that QLCSs (and their local environments) can be sampled with targetable ground-based instrumentation in a region not traditionally considered optimal for tornadogenesis studies (because hilly and forested terrain and sometimes sparse road networks result in a nonoptimal setup for a traditional “storm chasing” approach). The large spatial scale and longevity of QLCSs prove advantageous for deploying nonchasing instrumentation in this region; a targeted network can be deployed to prescouted locations several hours in advance of a forecast QLCS, with a high likelihood of useful data collection. The 2016–18 VSE campaigns were highly instructive, but they did not specifically use a strategy optimized for QLCSs, and they were undertaken with instrumentation that varied greatly from case to case.

Building upon the results and lessons learned from these previous VSE projects, and in light of the gaps in the current understanding of QLCS tornadogenesis, the Propagation, Evolution, and Rotation in Linear Storms (PERiLS) project was conceived as a focused observational field campaign that utilized a dense, tightly integrated network of instrumentation to sample QLCSs and the local environments in which they form. PERiLS is a collaborative effort between the National Science Foundation (NSF) and NOAA researchers.

2. Major outstanding scientific questions concerning QLCS tornadoes

QLCS tornadoes often develop within parent centers of vertical vorticity (“mesovortices”; e.g., Trapp et al. 1999; Davis and Parker 2014). Although there has been some recent convergence toward an accepted pathway for supercell tornadogenesis (e.g., Markowski et al. 2002; Markowski et al. 2012; Kosiba et al. 2013), it is unclear how well these mechanisms apply to mesovortices and tornadogenesis in QLCSs. A variety of possible QLCS tornadogenesis mechanisms have been advanced, most of which were formulated from simplified numerical modeling studies. Attempts at observational studies of QLCS vortices and tornadoes are few, and, when attempted, have been particularly hindered by the vortices’ and tornadoes’ apparent small size, low predictability, and/or transience.

The operational challenges posed by QLCS tornadoes are more acute in the SE due to their frequent occurrence within large-scale nocturnal and cool-season environments, having large low-level vertical wind shear and marginal instability [“high-shear, low-CAPE” (“HSLC”) large-scale environments]. Often, with this large low-level vertical wind shear, there is an overlap in large-scale QLCS and supercell environments (Anderson-Frey and Brooks 2019) and storm mode can be mixed (Smith et al. 2012; Thompson et al. 2012; Sherburn and Parker 2019). The relative role of the local environment (which can contain variations due to local effects such as terrain, differential heating, and previous and ongoing convection) versus the large-scale forcing in determining storm mode is unclear. HSLC environments are prevalent in the SE and mid-Atlantic regions of the United States, and storms that form in these environments account for a substantial fraction of severe wind and tornado reports in these regions (e.g., Schneider and Dean 2008; Sherburn et al. 2016). Observational and modeling studies investigating HSLC QLCSs thus far have been comprised of simulations of limited scope (e.g., Wheatley and Trapp 2008; Sherburn and Parker 2019) or have involved simple comparisons of environments (Sherburn and Parker 2014; Sherburn et al. 2016). As of yet, there has been no beginning-to-end explanation of the chain of events which leads to HSLC QLCS tornadogenesis, nor how, specifically, these processes are linked to the local environment of the QLCS.

The PERiLS field campaign sought to gather data to address the following objectives: 1) Identify the mechanisms for low-level mesovortex formation; 2) identify the characteristics and mechanisms that distinguish tornadic from nontornadic QLCS mesovortices; 3) identify the local environmental variability and local storm–environment interactions that are associated with QLCS mesovortex and tornado formation; and 4) characterize the role of system-generated cold pools in the evolution of strongly forced QLCSs.

a. Low-level vortexgenesis. QLCS simulations suggest that vertical vorticity within a QLCS's outflow is generated via the tilting of horizontal vorticity generated either by baroclinicity (e.g., Trapp and Weisman 2003; Wakimoto et al. 2006; Wheatley and Trapp 2008; Atkins and St. Laurent 2009) or by friction (e.g., Schenkman et al. 2012; Parker et al. 2020). While most studies suggest that baroclinic vorticity is tilted by a downdraft (e.g., Trapp and Weisman 2003; Wakimoto et al. 2006; Wheatley and Trapp 2008), Atkins and St. Laurent (2009) found that under certain circumstances, baroclinic vorticity may be tilted by an updraft. These similarities to supercellular vortex formation are perhaps not surprising; in at least a subset of QLCSs, mesovortices appear to be associated with helical updrafts with at least some reflectivity features akin to supercells (e.g., Sherburn and Parker 2019).

Although processes in QLCS outflows are commonly implicated in these studies, there are still uncertainties about the most relevant sources of downdraft air linked to vortexgenesis (Atkins and St. Laurent 2009; Marquis et al. 2018). Parker et al. (2020) noted that mesovortices were attached to vortex lines originating in the outflow of both a highly idealized and a corresponding full-physics case study simulation. However, within the more-idealized framework, the baroclinic mechanism appeared to predominate, whereas within the less-idealized framework, frictional sources appeared to become important. This may mean that the omission of surface and boundary layer processes from idealized modeling studies of QLCSs is problematic. Without near-ground measurements of the winds within QLCS outflows, such uncertainties will be difficult to resolve. It is also conceivable that local environmental horizontal vorticity is a source for QLCS vortices (e.g., Wheatley and Trapp 2008; Atkins and St. Laurent 2009; Flournoy and Coniglio 2019). Unfortunately, this possibility is hard to generalize because many pioneering QLCS modeling studies used wind profiles with purely crosswise ambient vorticity (lessening contributions from updraft tilting of inflowing local environmental air).

Horizontal shearing instability (HSI) may also play a role in producing QLCS vortices (Carbone 1983). A recent study of two SE U.S. QLCSs (Conrad and Knupp 2019) suggested that, similar to mesovortex generation along cold frontal rainbands (e.g., Clark and Parker 2014), drylines (e.g., Marquis et al. 2007), lake-effect snowbands (e.g., Mulholland et al. 2017; Kosiba et al. 2019), and other boundaries (e.g., Buban and Ziegler 2016), HSI may be sufficient for vortexgenesis. However, only one of the QLCSs analyzed by Conrad and Knupp (2019) produced a tornado, and the rather coarse resolution and high altitude (1.2 km AGL) of their analyses did not depict the other small-scale low-level features that might also instigate or influence vortexgenesis. Although recent work by Goodnight et al. (2022) suggests that HSI is a precursor in perhaps only a third of QLCS tornado events, its actual role in tornadogenesis remains an open question.

b. Mesovortices associated with tornadoes. Similar to supercell tornadogenesis (Markowski et al. 2002; Kosiba et al. 2013; Markowski and Richardson 2014; Skinner et al. 2015; Coffey et al. 2017; Coffey and Parker 2017; Guarriello et al. 2018), the low-level vertical vorticity in QLCSs needs to be concentrated to tornadic strength. As with supercells, it is likely that most QLCS mesovortices are nontornadic (e.g., Trapp 1999; Trapp et al. 2005; Anderson-Frey et al. 2016), although this frequency is not well documented. Nontornadic mesovortices can

still produce severe straight-line winds (Trapp and Weisman 2003; Wheatley et al. 2006), so identifying their formation mechanisms is nevertheless important. In addition to the uncertainty of how rotation originates in QLCSs, very little is known about why some QLCS mesovortices become tornadic.

Presumably, the properties of convective downdrafts and outflows are as important in QLCSs as in supercells, but such small-scale processes have never been directly observed in QLCSs. Sherburn and Parker (2019) found that vortex intensification in a simulated QLCS was closely linked to dynamical vertical accelerations (much as in supercells). McDonald and Weiss (2021) found no obvious differences in the thermodynamic deficits of the tornadic and nontornadic outflows they studied during VORTEX-SE, but they did note that two QLCS events exhibited stronger temperature gradients near tornadic mesovortices than near nontornadic mesovortices or other segments of the convective line. Generalizing these findings requires a larger sample of QLCSs, including dual/multi-Doppler wind retrievals to depict relevant processes. Even weaker vortices embedded in intense winds associated with QLCS may cause tornadic-intensity damage (e.g., Mahale et al. 2012).

c. QLCS environment. The strength and lifetime of QLCS mesovortices appear to be primarily dictated by the low-level local environmental shear vector magnitude (Weisman and Trapp 2003; Schaumann and Przybylinski 2012). In contrast to supercells, mesovortices within QLCSs are typically more transient and shallower (e.g., Trapp and Weisman 2003; Weisman and Trapp 2003; Wakimoto et al. 2006; Atkins and St. Laurent 2009; Davis and Parker 2014; Xu et al. 2015). The mesovortices that do produce tornadoes and/or damaging straight-line winds tend to be longer lived, taller, and stronger than nonsevere mesovortices (e.g., Przybylinski et al. 2000; Atkins et al. 2004, 2005; Lovell and Parker 2022), characteristics that appear to be correlated with the low-level shear vector magnitude (Weisman and Trapp 2003; Trapp et al. 2005; Schaumann and Przybylinski 2012). The typically large values of low- to mid-level shear vector magnitude in HSLC environments may therefore explain why a large fraction of QLCS tornadoes occur within HSLC convection (Smith et al. 2012; Davis and Parker 2014).

Sherburn and Parker (2019) examined the impacts of varying low-level shear and stability upon simulated QLCSs with “embedded supercells” (having at least temporarily distinguishable supercell-like structures). They found that both stability and low-level shear had a direct impact on the strength of the lower-tropospheric updraft and subsequent intensification stretching needed to produce a possibly tornadic vortex. Perhaps not surprisingly given limited CAPE, the dynamical accelerations linked to the low-level shear outpaced those associated with buoyancy in their simulated QLCSs. Even so, Sherburn and Parker (2019) noted “that many QLCS tornadoes are likely associated with bow-echo type structures and mesovortices, which likely differ physically from the supercellular mechanisms discussed herein.” In addition, Sherburn et al. (2016) found that the mean HSLC severe event had stronger large-scale forcing (upper tropospheric troughs, surface cyclones, and surface fronts) and ascent than its nonsevere counterpart, implying that local convective ingredients alone may be insufficient to fully characterize the threat.

Case study simulations by King et al. (2017) showed that the most severe events experienced comparatively large destabilization, an increase in CAPE by over 400 J kg^{-1} in 3 h, relative to the nonsevere events. The footprint of the destabilization was often surprisingly small, sometimes less than 100-km wide. Such rapid and narrow structures have never been targeted with an observational campaign. Murphy et al. (2022) showed thermodynamic and kinematic profiles evolved rapidly in the 30–60 min prior to a tornadic QLCS in northern Louisiana in 2020, underscoring the importance of high temporal local environmental sampling. Mesoscale spatial variability in the form of a preexisting boundary (e.g., remnant

outflow from prior storms) has been shown to strongly affect subsequent QLCS strength and evolution (e.g., Lombardo 2020; Wu and Lombardo 2021) and provide a focus for mesovortex and tornadogenesis in both supercells (e.g., Atkins et al. 1999) and QLCSs (e.g., Przybylinski et al. 2000). It is unclear what kinds of storm–boundary interactions are most beneficial, nor what is the failure rate for vortexgenesis during such interactions.

d. Cold front and cold pool processes. Most QLCS literature has focused on systems that self-organize along system-generated cold pools (e.g., Houze 2018), but many SE QLCSs are linked to strong cold frontal forcing (Sherburn et al. 2016; King et al. 2017). A final gap in the knowledge base is the degree to which these systems operate as traditional, cold pool-driven MCSs versus frontally driven precipitation systems. Jewett and Wilhelmson (2006) noted that large-scale forcing could continue to influence simulated convection throughout its lifetime, including producing a strong bias toward more cyclonic vortices. There is also an interesting resemblance to the attributes of the narrow cold frontal rainbands (NCFRs) described by Hobbs and Persson (1982), including a correspondence between the “core and gap” structure of Hobbs and Persson (1982) and the “broken S” structure thought to commonly describe severe QLCSs (e.g., Davis and Parker 2014).

The working assumption is that essentially all SE QLCSs possess evaporatively produced cold pools that cause them to move ahead of the synoptic cold front over time. However, there have never been concerted measurements of the degree of separation/interaction between identifiable QLCS cold pool processes and identifiable cold frontal processes. These gaps in knowledge are particularly important in the HSLC environments of the SE, where instability is often weaker and synoptic forcing is often stronger.

3. The PERiLS field experiment

PERiLS deployed a diverse array of instruments (Fig. 1) to sample the pre-QLCS environment, QLCS evolution, and its interaction with the local environment. A list of the instruments deployed for PERiLS (and affiliated institutions) is provided in the appendix.

While the overall length of a QLCS may be hundreds of kilometers, there is great uncertainty concerning where a QLCS is most likely to produce mesovortices, tornadoes, and/or severe winds. Arrays of mobile X- and C-band radars, mobile mesonets, deployable instrumentation, soundings, and UAS have been used in prior targeted/adaptable tornado and mesoscale projects (e.g., VORTEX2, Wurman et al. 2012; PECAN, Geerts et al. 2017; and RELAMPAGO, Nesbitt et al. 2021). However, PERiLS presented experimental designers with different and difficult challenges. Traditional scientific chasing of convective systems (e.g., VORTEX2 or PECAN, where ad hoc arrays of radars and other instruments were determined immediately prior to data collection) was not practical or safe in the SE due to irregular road networks, many small towns, trees, hills, the fast motions of the QLCSs themselves, the relatively long setup time of extensive in situ arrays, and the lead time necessary for additional NWS soundings and Federal Aviation Administration (FAA) approvals for UAS. Therefore, each PERiLS intensive operations period (IOP) employed a customized nonchasing, prescouted radar array, placed in advance of convective arrival to span a substantial portion of the forecasted QLCS. This maximized the chances of high-quality near-ground radar sampling of features associated with severe winds and/or tornadoes.

Based on previous VSE operations and surveys, 10 geographical subdomains within the larger PERiLS observational domain were identified (Fig. 2). To establish the backbone multiple-Doppler radar networks in each subdomain, candidate sites with minimal horizon blockage were identified, with over 200 sites preselected as possibly suitable for PERiLS (Fig. 3). The University of Illinois at Urbana-Champaign (UIUC) Flexible Array of Radars and Mesonets (FARM) team worked with assistance from members of the Geo Experience Center



FIG. 1. Some of the instruments used during PERILS: (a) UAH MIPS, (b) ULM DWL, (c) OU CopterSonde, (d) NSSL/CIWRO UAS, (e) SBU preparing a SwarmSonde, (f) UIUC/NCSU sounding launch, (g) sounding being launched at the OU CLAMPS, (h) UIUC wind profiler, (i) NSSL MM, (j) UIUC MM and Pod, (k) Purdue PIPS, (l) TTU StickNet being set up, (m) NSSL LMA being set up, (n) UIUC COW radar being set up, (o) UIUC COW radar ready to operate, (p) OU SMART-R radar deployed, (q) UIUC DOW7 radar deployed, (r) NSSL NOXP radar deployed, and (s) UAH MAX radar deployed.

team at Esri to develop experimental site-evaluation software that employed fine-scale lidar mapping of terrain and land cover, providing a substantial advantage over terrain-height-only models (hill finders) (Fig. 4). Horizon visibility was evaluated in azimuthal sectors along most paved roads in several of the subdomains, at intervals of 100 m along the roads. Site quality was evaluated subjectively using the azimuthal distribution of horizon visibility in sectors likely to be used for multiple-Doppler retrievals. Since construction after the lidar mapping, vehicles, and other factors caused some errors in automatic evaluation, on-site validation was performed for all candidate sites. Many potential sites were also clutter-surveyed with an X-band radar. Ease of access, mud, flooding potential, landowner permission, and cellular telephone coverage were additional considerations in siting. From the selected sites, at least two multiple-Doppler radar configurations were constructed for each subdomain (Fig. 3).

a. Data collection phase. The PERiLS data collection period was initially scheduled for 2021 and 2022, but was pushed back to 2022 and 2023, due to disruptions related to COVID-19. Operations ran from 1 March to 1 May 2022 (“year 1”) and 8 February to 8 May 2023 (“year 2”). The longer operation period in year 2 facilitated the capture of more early-season events.

b. Observational strategies. Each IOP’s observing domain was selected by weighting a combination of factors, including the forecasted QLCS location, timing, and the quality of the radar network available in each PERiLS subdomain.

PERiLS Domain and Subdomain Reference Towns

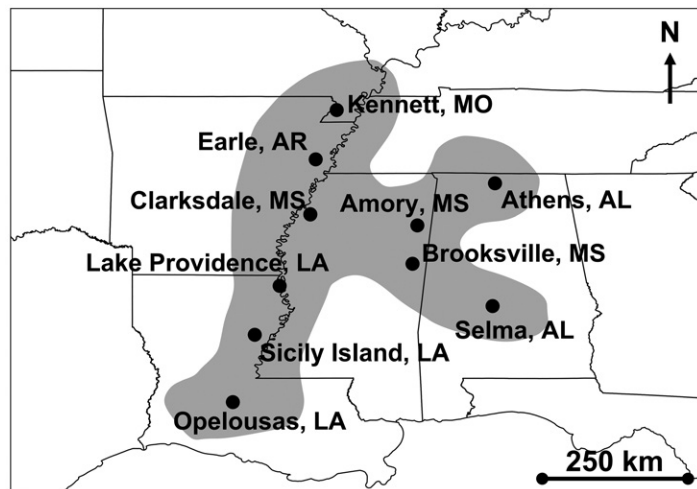


FIG. 2. Outline of the PERiLS domain and locations of the 10 reference communities that anchored the operation subdomains. The delta domains encompass Opelousas, Louisiana, to Kennett, Missouri; the black belt domains encompass Selma, Alabama, to Amory, Mississippi; and the Tennessee Valley domain encompasses Athens, Alabama.

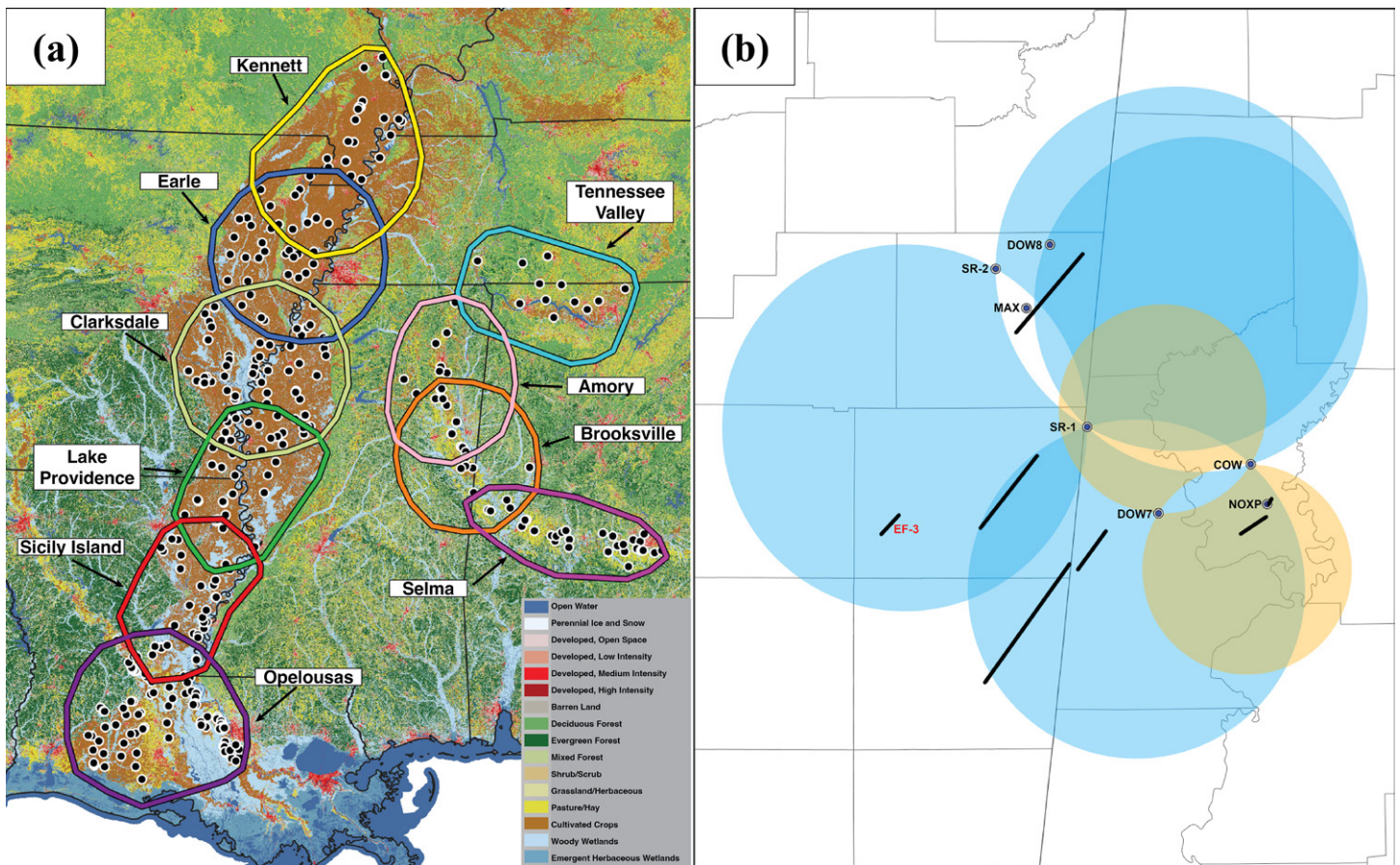


FIG. 3. (a) PERiLS subdomains (colored lines) and surveyed radar sites (black dots). Subdomains are as follows: Yellow is Kennett; blue is Earle; olive is Clarksdale; green is Lake Providence; red is Sicily Island; purple is Opelousas; cyan is Tennessee Valley; pink is Amory; orange is Brooksville; and magenta is Selma. (b) PERiLS radar configuration used for IOP1 in year 1 in the Brooksville subdomain [orange polygon in (a)]. The blue dots indicate the location of the radars; the 30°-C-band dual-Doppler lobes are shown in cyan; yellow depicts the 30°-DOW7-COW dual-Doppler lobes, which remained in place for the duration of the IOP. Tornadic vortices tracked by the COW radar during this IOP are shown with black lines.

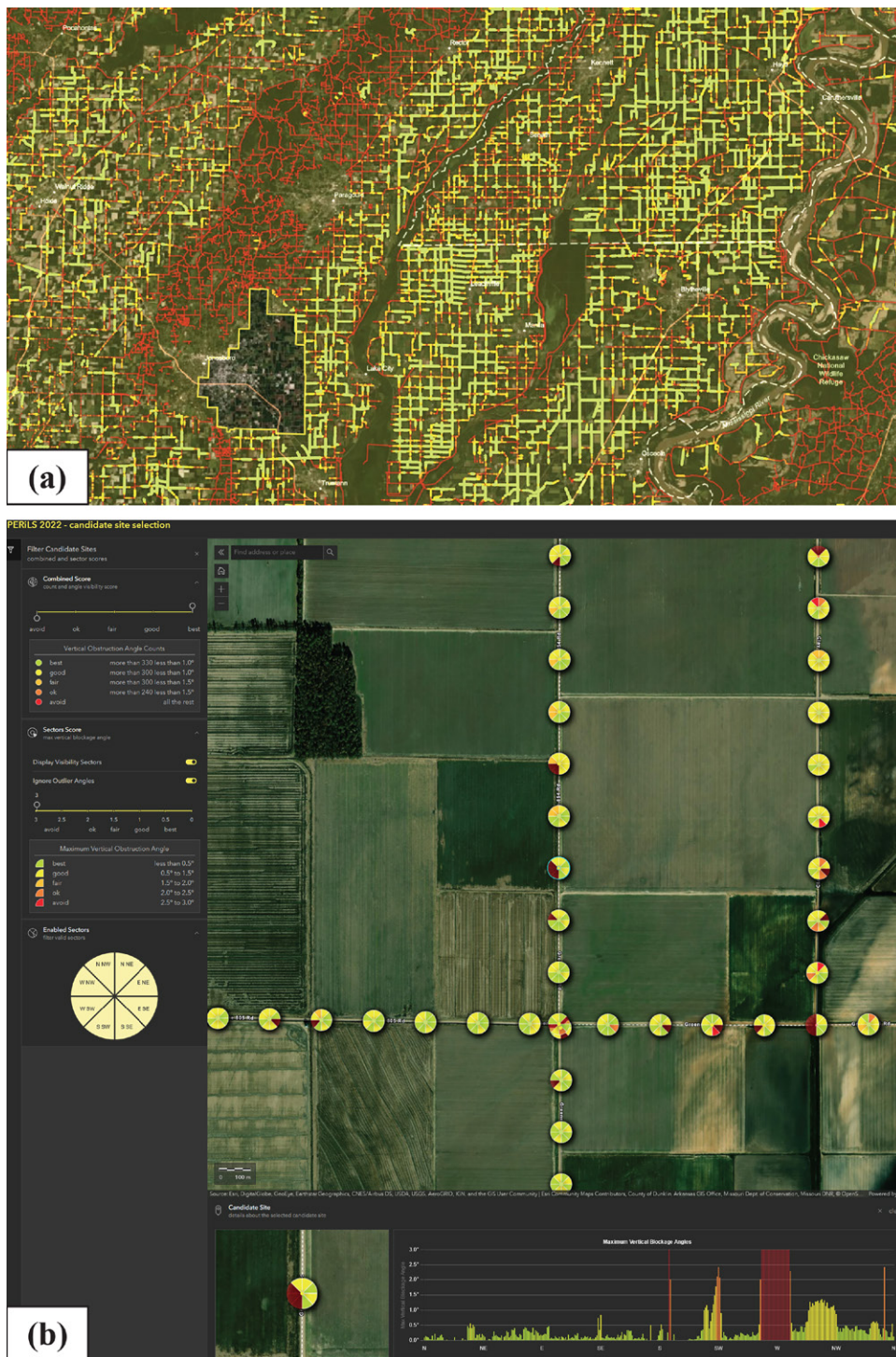


FIG. 4. Site selection tool. (a) Large-area view illustrating site-rich/poor regions as rated based on lidar mapping, with good sites colored green, through poorly rated red sites. (b) Small-area view illustrating pie chart sector-average horizon visibility scoring for sites spaced at 100-m intervals, and (bottom right) fine-azimuthal scale blockage scoring highlighting narrow blockage from, e.g., power poles and individual trees, and (bottom left) zoomed-in aerial view.

The specific siting of instruments then was designed with the following considerations for each unique IOP.

1) NESTING OF C- AND X-BAND RADAR ARRAYS. Mobile and quickly deployable C-band radars were chosen for the backbone multi-Doppler network for PERiLS in order to mitigate the effects of attenuation suffered by 3-cm (X-band) systems (e.g., Doviak and Znić 1984; Wurman et al. 2012; Geerts et al. 2017). The C Band on Wheels (COW) (Wurman et al. 2021),

Small Missions for Advanced Research in Technology (SMART)-R1, and SMART-R2 (Biggerstaff et al. 2005) were deployed in bent lines at ~35-km spacing (Fig. 3b). Optimally, the COW was the central C-band radar since it has higher power [two 1-MW transmitters vs one 250-kW transmitter] and has a narrower beam than the SMART-Rs, but this arrangement varied depending on the availability of COW-compatible sites (the COW requires a cleared area of about 6 m × 10 m to allow for antenna assembly). Embedded in the C-band network were three X-band radars, DOW7 (Wurman et al. 2021), NOXP (Palmer et al. 2009), and MAX (Asefi-Najafabady et al. 2010). In practice, the X bands were used to cover C-band baselines, extend the network, and fill in for missing radars. Because of attenuation, baselines with X-band radars usually were <25 km, whereas the baselines between C-band radars usually were <35 km. During some IOPs, specifically IOPs 1–4 in 2022 and IOPs 4 and 5 in 2023, DOW6 and/or DOW8 added additional X-band coverage to the network.

A challenge during several of the IOPs was the proximity of potentially tornadic circulations to the particular radars within the radar array. Occasionally, some of the radar operators assessed that tornadoes would impact their radar locations, so they evacuated their sites. In these circumstances, radars were either left running unattended or driven away, and then back to their sites when the operators assessed that they were safe. When feasible, DOW6/8 also was used in a nomadic mode to mitigate the loss of coverage from radar departures.

Both the C and X bands adapted a coordinated, synchronized scan strategy for multi-Doppler analyses when convection was within the domain. In year 1, the low levels were revisited every 180 s (3 min). After evaluation of the year 1 data, it was decided that this update time should be shortened to 90 s (1.5 min). From the 3D winds, quantities such as shear and vorticity, and their forcings such as stretching and tilting of vorticity, can be calculated and used to assess processes that contribute to low-level vortexgenesis. With suitably long/contiguous observations, trajectories can be computed to diagnose the path of air parcels, along with the local environmental forcings experienced along those paths (e.g., Kosiba et al. 2013). Single-Doppler observations permit the examination of rapidly evolving features and the diagnosis of cold pool depth. Dual-polarimetric fields, alone and in conjunction with trajectories, can be used to infer microphysical processes, which can be related to updraft and downdraft properties.

In addition to the multi-Doppler network, two rapid-scan radars, RaXPol (Pazmany et al. 2013) and Skyler (Kollias et al. 2018), were deployed during year 2, focusing on observing the rapid evolution of low-level storm features. RaXPol and Skyler operated in a more traditional, quasi-mobile manner, with sites chosen opportunistically for each IOP to collect targeted, close-range observations of mesovortices and other rapidly evolving storm features. The rapid-scan radars coordinated with other PERiLS assets, when possible, to supplement the larger multi-Doppler network and other targeted measurements.

2) SURFACE IN SITU OBSERVATIONS. A dense, 2D network of surface assets, which included the Texas Tech University (TTU) StickNet (Weiss and Schroeder 2008), the UIUC FARM Pods (Wurman et al. 2021), and UIUC FARM and NSSL mobile mesonet vehicles, was deployed within the mobile radar coverage. Dense surface observations were necessary to diagnose inflow and cold pool heterogeneities and perturbations, which varied both along lines and with time. Thermodynamics of cold pool air, also sampled with soundings, allowed for the assessment of air parcel origins to help diagnose internal storm processes that may influence tornadogenesis, as it has been suggested that subsystem scale updrafts and downdrafts may be influential, and potentially preferred locations, for tornadogenesis. Additionally, baroclinicity along inflow/gust front interfaces can be assessed, and this, along with vorticity derived from the 3D winds, can provide evidence for mechanisms leading to tornadogenesis.

Prior to the start of PERiLS, and based on previous operations during VSE, over 300 sites were scouted for the StickNet probes. Due to the setup time of the large array, which included recontacting landowners, the initial 16 members of the 24-member StickNet were deployed 24–36 h in advance of the IOP, after the determination of the final radar configuration (see section 4d). By default, this “coarse” array of StickNet members was arranged in a 4×4 grid, with ~ 30 -km spacing between instruments, centered on the location where the center C-band radars were to be deployed. Within the coarse StickNet array, a smaller, finer spatial resolution array was deployed within an hour prior to the arrival of the QLCS. This array comprised eight StickNet probes and 13 Pods deployed by the UIUC FARM, which were commonly deployed before mesonet transects commenced. The fine array of StickNet probes was deployed with 1-km spacing, and Pods were typically deployed in a linear array with 3-km spacing. The coarse array was intended to resolve mesoscale heterogeneities within both the inflow and cold pool. The finer arrays allowed for a sampling of local environmental heterogeneities near ground for convective structures, and the timing allowed for precise positioning based on the most recent forecasts and observations.

The three UIUC FARM mobile mesonets (MMs) were responsible for deploying the Pods [and three disdrometers; see section 3b(3)(i)] premission and then transitioned to their IOP mission, which was to measure the QLCS local environment, gust front, and cold pool using line-perpendicular transects across the gust front. The transects were separated by ~ 25 km (highly dependent on road networks and line orientation), allowing for sampling of spatial variability in the cold pool, gust front, and local environment. Depending on storm evolution, the transect paths of the MMs were altered in real time.

Two NSSL MMs focused on collecting data to improve understanding of surface thermodynamics and kinematics in close proximity to QLCS mesovortices. To achieve this goal, the NSSL MMs positioned themselves in tandem ahead of a segment of the QLCS where mesovortices were either ongoing or appeared possible. Before the arrival of a segment, the MMs would diverge out of their path in opposite directions. Once the vortex crossed the target highway, each MM would return to the starting position, thus completing a closed circuit of observations in a storm-relative frame of reference surrounding the target segment.

3) MICROPHYSICAL AND LIGHTNING MEASUREMENTS. All of the coordinated Doppler radars conducted two mid- to high-level scans designed to sample broad areas of the QLCS above the melting layer. This facilitated monitoring of the microphysical properties of the mixed-phase layer and its relationship with storm dynamics and provided a baseline for microphysical and lightning analyses.

(i) Disdrometers. Optical disdrometer observations yield direct measurements of the particle size and fall velocity, complementing and serving as a basis for validation and improvement of drop size distribution (DSD) retrieval algorithms applied to dual-polarimetric radar data. DSD and their variability in convective storms 1) are intimately connected with cold pool strength via evaporative cooling (e.g., Dawson et al. 2010; Bryan and Morrison 2012) and 2) provide information about the near-surface kinematics through size sorting by updrafts and storm-relative winds (e.g., Kumjian and Ryzhkov 2012; Dawson et al. 2015). Both are likely to be strongly linked to tornadogenesis in QLCSs, especially regarding how they impact baroclinic vorticity generation and near-surface convergence along the gust front.

Purdue fielded six Portable In Situ Precipitation Stations (PIPS). The PIPS are equipped with conventional surface instrumentation (temperature, relative humidity, pressure, and wind speed and direction) and OTT Parsivel² laser disdrometers (Löffler-Mang and Joss 2000; Tokay et al. 2014). In close coordination with the StickNet teams, the PIPS were deployed in a “picket fence” formation with spacings $O(5\text{--}20)$ km ahead of and parallel

to an approaching QLCS. Depending on the perceived need for improved DSD statistics and/or instrumentation comparisons, occasionally two PIPS would be collocated. The UIUC FARM deployed an additional three OTT Parsivel² laser disdrometers, each collocated with a Pod (to also obtain collocated temperature, relative humidity, pressure, wind speed, and direction) within the C-band multi-Doppler array.

(ii) Lightning mapping arrays. Total lightning observations, including cloud-to-ground and intracloud flashes, may allude to local environmental favorability for generating updraft structures which can become capable of sustaining rotation in a QLCS. High-resolution, three-dimensional, and continuous lightning observations are key for highlighting rapid variations in updraft perturbations (e.g., Mecikalski and Carey 2017; Salinas et al. 2022) and monitoring mixed-phase precipitation volumes (e.g., Vincent et al. 2003; Liu et al. 2012; Sharma et al. 2021). Total lightning trends can signal the evolution of storm downdrafts (e.g., Goodman et al. 1988; Williams et al. 1999) and downdraft-driven vorticity (Stough et al. 2017). Lightning mapping arrays (LMAs; Rison et al. 1999) provide this context, mapping the full propagation of lightning channels with high accuracy near the network (Thomas et al. 2004; Koshak et al. 2004) with real-time capabilities. LMAs additionally serve as an underlying link between the operationally available lightning datasets, which each observe different portions of the discharge process with their own inherent restrictions and biases.

Prior to the project, sites for the eight sensors in the NSSL/TTU LMA were scouted in each of the PERiLS subdomains. Sites were targeted to be 20–40 km apart, depending on road networks and geography, to optimize minimizing deployment time and improving network accuracy (e.g., Koshak et al. 2018). Sites were visited in person to meet with landowners, evaluate line of sight for antennas, determine likely feasibility of site access after storm passage for retrieval, and test for background very high frequency (VHF) radio noise. Potential LMA networks were optimized for each subdomain using Monte Carlo simulations (Chmielewski and Bruning 2016). Potential networks produced coverage areas of at least 90% flash detection efficiency and altitude errors less than 1 km within the surrounding 100 km, approximately the size of many of the subdomains, with many networks expected to be significantly more sensitive.

Following the determination of the radar configuration, the eight-sensor LMA was deployed to the nearest optimal array configuration and was operational no later than 3 h prior to IOP start. Modifications were made to the array configurations as needed due to changes in local VHF noise levels or site access between the time of initial scouting and the time of deployment.

4) SOUNDINGS. Observations and simulations suggest large-scale HSLC environments can support mixed convective modes, and this may be determined not only by the local environment but also by the larger-scale forcing and its orientation with respect to the wind profile (e.g., Dial et al. 2010). Numerical simulations have suggested that potentially hazardous QLCS structures (such as mesovortices and bowing segments) may result either from local environmental heterogeneities or from self-organized structures and processes attributable to QLCSs themselves. Further, the rapid evolution of the local environment may occur in the hours prior to QLCS arrival (e.g., Lombardo 2020).

PERiLS deployed a nested network of moveable sounding systems to sample the local environment before and after convection at unprecedented spatial and temporal evolution to capture heterogeneities and the effects of large-scale advection and lifting. This network was uniquely designed for each IOP, combining a broader array of six to seven sounding systems that spanned most of the dual-Doppler radar observing domain with a denser subarray of four sounding systems that were spaced roughly 25 km from one another in the same vicinity

as the surface pod and MM operations. The soundings within the broader array were begun roughly 4 h before the expected arrival of the target QLCS, with a time spacing of roughly 60–120 min. Soundings within the denser subarray were begun close to the time when the target QLCS was expected to enter the dual-Doppler radar observing domain, with a time spacing of roughly 30–60 min. Many of these sounding systems continued launches at regular intervals well into the QLCS cold pool, often until the trailing end of precipitation had passed through the array (and occasionally, until the approach of the synoptic cold front, if sufficiently close by).

While the majority of these soundings spanned the depth of the troposphere, some of the sounding systems used lighter balloons that were primarily suitable for measuring the lower-tropospheric evolution. Given the PERiLS goals of depicting rapid evolution in the low-level stability and wind profiles, as well as the properties of the system's cold pools, having more frequent launches focused on the lowest several kilometers of the troposphere proved quite beneficial. The nested network profitably combined the broader array's longer observing period with the denser subarray's finer spatial and temporal resolution, serving to capture both regional-scale variability and local details in the immediate vicinity of mesovortices and other interesting QLCS features.

Hourly soundings occasionally continued through until after the passage of the final synoptic cold front to help delineate the roles of QLCS-generated cold pools from the roles of synoptic cold fronts (along which the QLCSs usually were initially formed). These soundings, along with high-resolution surface observations (discussed previously), were used to characterize and distinguish the different air masses to aid in the identification of the relative roles. In practice, the combination of pre-QLCS and within-QLCS sampling required extended duty cycles, so the need for crew rest necessitated discontinuation of sounding observations and retrieval of many surface stations prior to the cold front's arrival. Nevertheless, the coarse StickNet array and routine NWS stations may prove useful in extending the surface dataset through the final frontal passage.

NSSL and Pennsylvania State University (PSU) also conducted a SwarmSonde mission (Markowski et al. 2018; Bartos et al. 2022) to examine QLCS inflow local environment evolution and spatial heterogeneities. Timed deployments began approximately 100 km downstream of the target QLCS where sondes were launched in 3-min intervals from a fixed position as long as conditions were favorable. This allowed 3-km horizontal resolution of the inflow local environment, in addition to capturing potential thermodynamic or kinematic heterogeneities. Coordinated launches were conducted when available, placing one team down the surface wind vector from the other to add a second vertical layer of observations within the inflow local environment.

5) ADDITIONAL ENVIRONMENT MEASUREMENTS. To more fully characterize the QLCS environment, PERiLS also deployed CopterSondes, the Collaborative Lower Atmosphere Mobile Profiling System (CLAMPS; Wagner et al. 2019), Atmospheric Sounder Spectrometers by Infrared Spectral Technology (ASSIST; Rochette et al. 2009), Doppler wind lidars (DWLs), and radar wind profilers (RWPs).

(i) CopterSonde. The University of Oklahoma (OU) CopterSonde is a custom-built, weather-sensing uncrewed aerial system designed specifically for precision thermodynamic and kinematic measurements in the atmospheric boundary layer (Segales et al. 2020; Bell et al. 2020), equipped with three iMet-XF bead thermistors and three HYT-271 relative humidity sensors, using a “wind-vane” algorithm to rotate the nose of the aircraft into the wind (Segales et al. 2020). Wind speed and direction are measured using the tilt of the aircraft and the tilt direction. The wind speed tolerance is 22 m s^{-1} . The CopterSonde platform went through an extensive airworthiness process in order to fly under a NOAA mission.

For PERiLS, the CopterSonde sites stayed fixed throughout the project and did not follow the rest of the armada, operating from Lake Village, Arkansas (AR); Schlater, Mississippi (MS); and Yazoo City, Mississippi. Primary site choice considerations were being away from busy airspace and military operating areas and densely populated areas. Working closely with NOAA, Certificates of Authorization (COAs) were acquired from the FAA to fly to 5000 ft (~1500 m) AGL day or night.

CopterSonde performed 360 flights over eight IOPs. During an IOP, flights occurred every 30 min, but typically the interval was decreased to every 15 min as storms or interesting mesoscale features approached. Flight periods were limited to 8-h total to limit operator fatigue.

(ii) CLAMPS. In Lake Village and Yazoo City, a trailer-based CLAMPS (Wagner et al. 2019) facility was collocated with CopterSonde flights. CLAMPS includes a Halo Photonics Stream-Line XR scanning Doppler lidar (Pearson et al. 2009), an Atmospheric Emitted Radiance Interferometer (AERI; Knuteson et al. 2004), and an RPG Humidity and Temperature Profiler (HATPRO) microwave radiometer (Rose et al. 2005). Thermodynamic profiles from the AERI and microwave radiometer (MWR) were retrieved using the Tropospheric Remotely Observed Profiling via Optimal Estimation (TROPoe) algorithm (Turner and Löhnert 2021; Turner et al. 2022).

(iii) ASSISTs. The ASSIST is a ground-based infrared spectrometer very similar to the AERI. Two ASSISTs were deployed during PERiLS, collocated with the RWPs in Columbia and Courtland. Thermodynamic profiles were retrieved at 10-min resolution or better from the ASSISTs using TROPoe.

(iv) Wind profilers. RWPs and DWLs were used to retrieve the wind profile and assess convective feedbacks on the local environmental wind in advance of QLCSs. PERiLS leveraged six deployable and fixed RWPs and DWLs, arranged in instrument-specific triangular configurations with baselines of ~40–60 km. All deployable profilers were collocated with an upper-air sounding system.

The 915-MHz RWPs were operated in a similar 6-azimuth beam configuration, using a high- and low-pulse repetition frequency mode at each beam, providing measurements from the lowest gate from 200 to 1500 and 1500 to 6000 m above radar level (ARL), respectively. Doppler spectra from successive measurements were coherently averaged for 5 min before calculating wind estimates.

Halo StreamLine XR DWLs were operated using an 8-point azimuth scan at 70° elevation every 5 min to facilitate VAD wind retrievals, with continuous vertically pointing stares in between. A 30-m gate spacing was utilized, with the lowest gate at approximately 60 m above lidar level and maximum range dependent on aerosol load or attenuation by larger particles. Maximum DWL ranges during PERiLS often exceeded 1000 m in the local prestorm environment.

Profilers were deployed at least 4 h prior to the estimated start of deep convection within the mobile radar dual-Doppler lobes and operated at least until overtaken by deep convection. In addition to the deployable profilers, NOAA operated five 915-MHz RWPs with radio acoustic sounding systems (RASS) for measurement of low-level temperature at sites near Courtland, Alabama; Columbia, Louisiana; Oakwood, Louisiana; Starkville, Mississippi; and Greenwood, Mississippi. MWRs and ceilometers were operated at the Courtland and Columbia sites. DWLs were also operated from the fixed CLAMPS sites in Lake Village, Arkansas; and Yazoo City, Mississippi.

6) DAMAGE ASSESSMENT. NSSL conducted ground, UAS, and satellite-based damage assessments to document the type and extent of high-wind damage. Following a high-wind event, NSSL deployed multiple damage survey teams to collect high-resolution imagery using multirotor copters and fixed-wing UAS platforms. PERiLS damage surveys were coordinated with

Tornadoes in PERiLS Instrumentation Networks

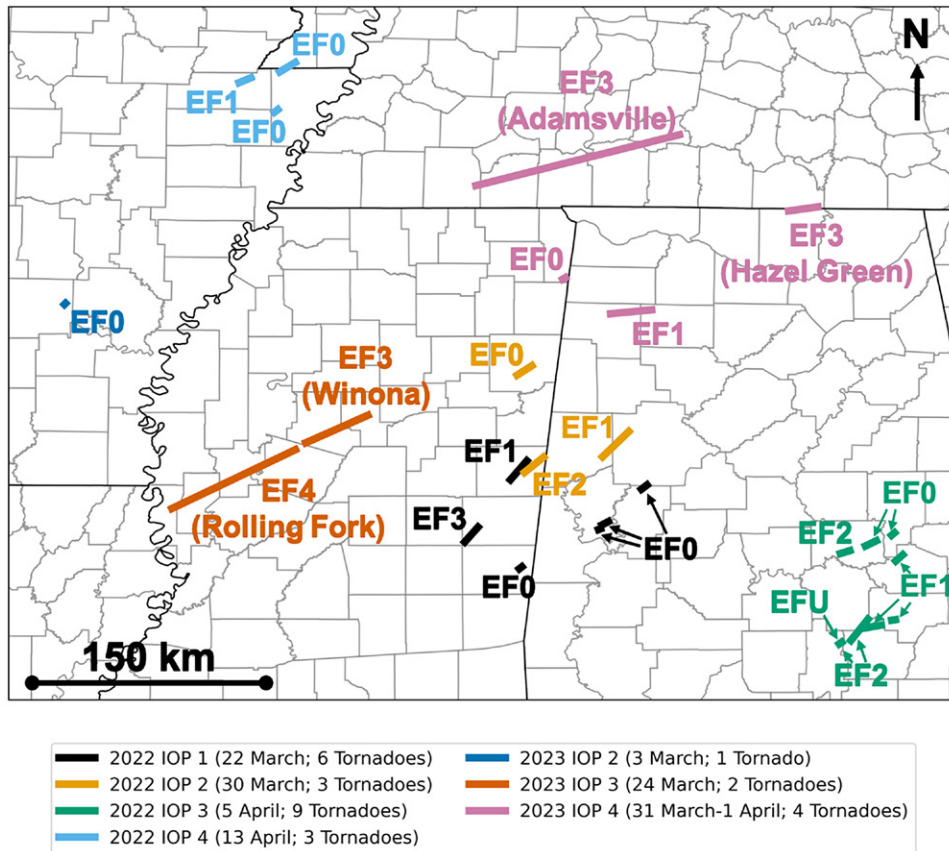


FIG. 5. Tornadoes within the PERiLS observation array. Black is year 1, IOP1; brown is year 1, IOP2; teal is year 1, IOP3; light blue is year 1, IOP4; dark blue is year 2, IOP2; orange is year 2, IOP3; and pink is year 2, IOP4. Tornadoes that were responsible for fatalities are denoted by the inclusion of communities impacted.

affected local National Weather Service (NWS) Warning Forecast Offices (WFOs) and, in the case of high-impact events, included coordinating satellite tasking and UAS missions with NOAA southern region and FEMA IV region. UAS and ground survey teams comprised NSSL/Cooperative Institute for Severe and High-Impact Weather Research and Operations (CIWRO) staff, students, and volunteers from NWS WFOs. High-wind damage information obtained from UAS, satellite, and ground surveys was shared with affected NWS WFOs. These data also are being analyzed and compared with the PERiLS radar network and other observational data.

TABLE 1. Dates, subdomain, and storm mode of the PERiLS IOPs.

| IOP | Date | Subdomain | Storm mode |
|------|--------------|----------------------|--|
| 2022 | | | |
| 1 | 22 Mar | Brooksville, MS | QLCS and supercell modes with EF0–EF3 tornadoes |
| 2 | 30 Mar | Amory, MS | QLCS with EF0–EF2 tornadoes |
| 3 | 5 Apr | Selma, AL | QLCS and supercell modes with EF0–EF2 tornadoes |
| 4 | 13 Apr | Kennett, MO | QLCS with EF0–EF1 tornadoes |
| 2023 | | | |
| 1 | 16 Feb | Brooksville, MS | QLCS with no observed tornadoes |
| 2 | 3 Mar | Clarksdale, MS | QLCS with an EF0 tornado |
| 3 | 24 Mar | Lake Providence, LA | QLCS and supercell modes EF3–EF4 tornadoes associated with supercell mode |
| 4 | 31 Mar–1 Apr | Tennessee Valley, MS | QLCS and supercell modes with EF0–EF3 tornadoes |
| 5 | 5 Apr | Kennett, MO | QLCS with no tornadoes |

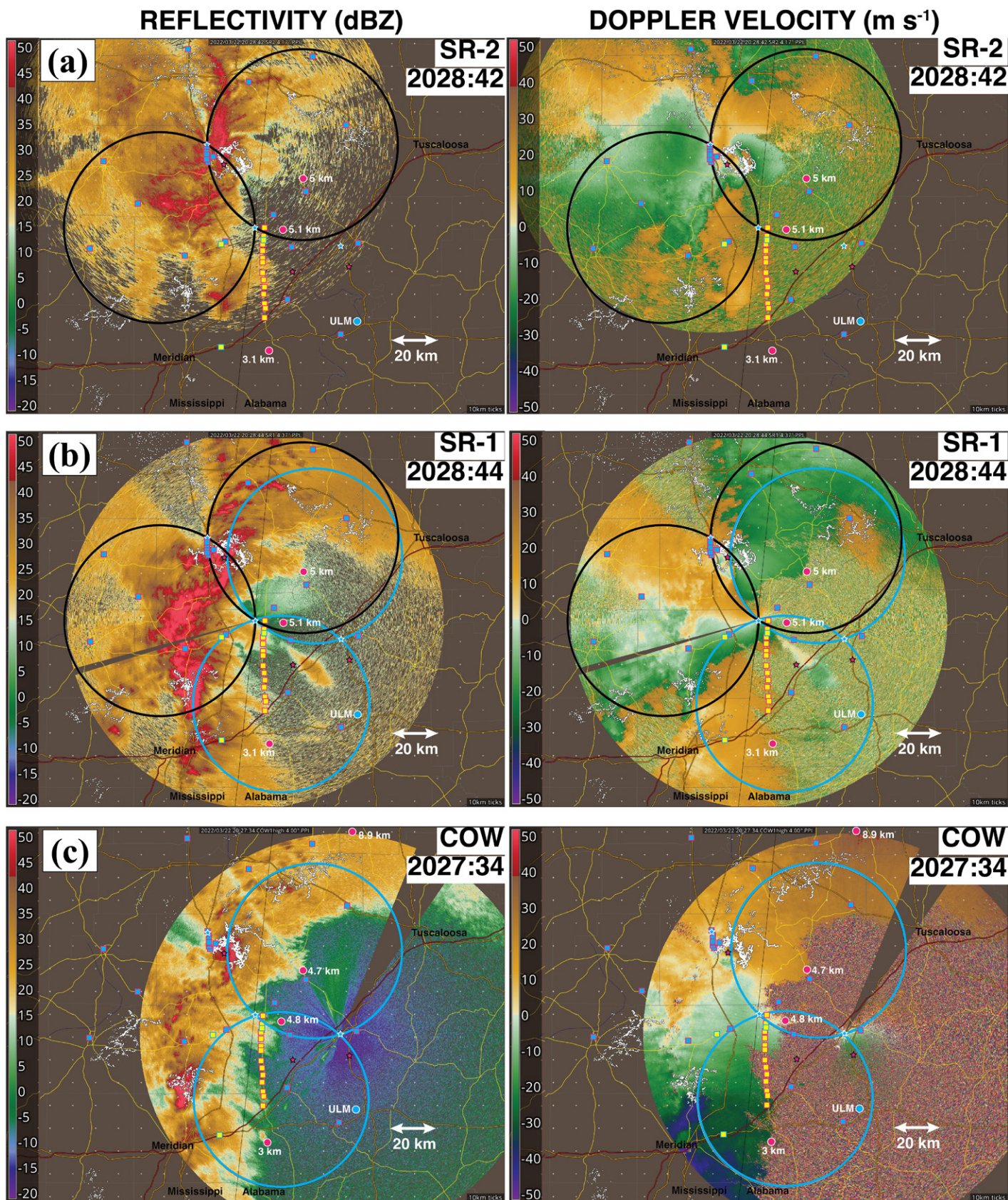


FIG. 6. Year 1, IOP1 deployment with select assets at about 2028 UTC 22 Mar 2022. C-band radar data are shown from (a) SR-2, (b) SR-1, and (c) COW. (left) Radar reflectivity; (right) the Doppler velocity product. The 30°-dual-Doppler lobes between SR-1 and SR-2 are shown in black; 30°-dual-Doppler lobes between SR-1 and COW are shown in blue. C-band locations are depicted with blue stars, and X-band locations are shown with pink stars. Surface assets are depicted with rectangles; yellow with pink outlines are pods; yellow with blue outlines are mesonets; and blue with pink outlines are Sticks. Soundings are shown with pink circles; altitude of the sounding at that location is given. The white circles are total lightning from the LMA within 7 s of the radar data. The Nyquist velocities are 24 m s^{-1} for SR-1 and SR-2 and 68 m s^{-1} for the COW.

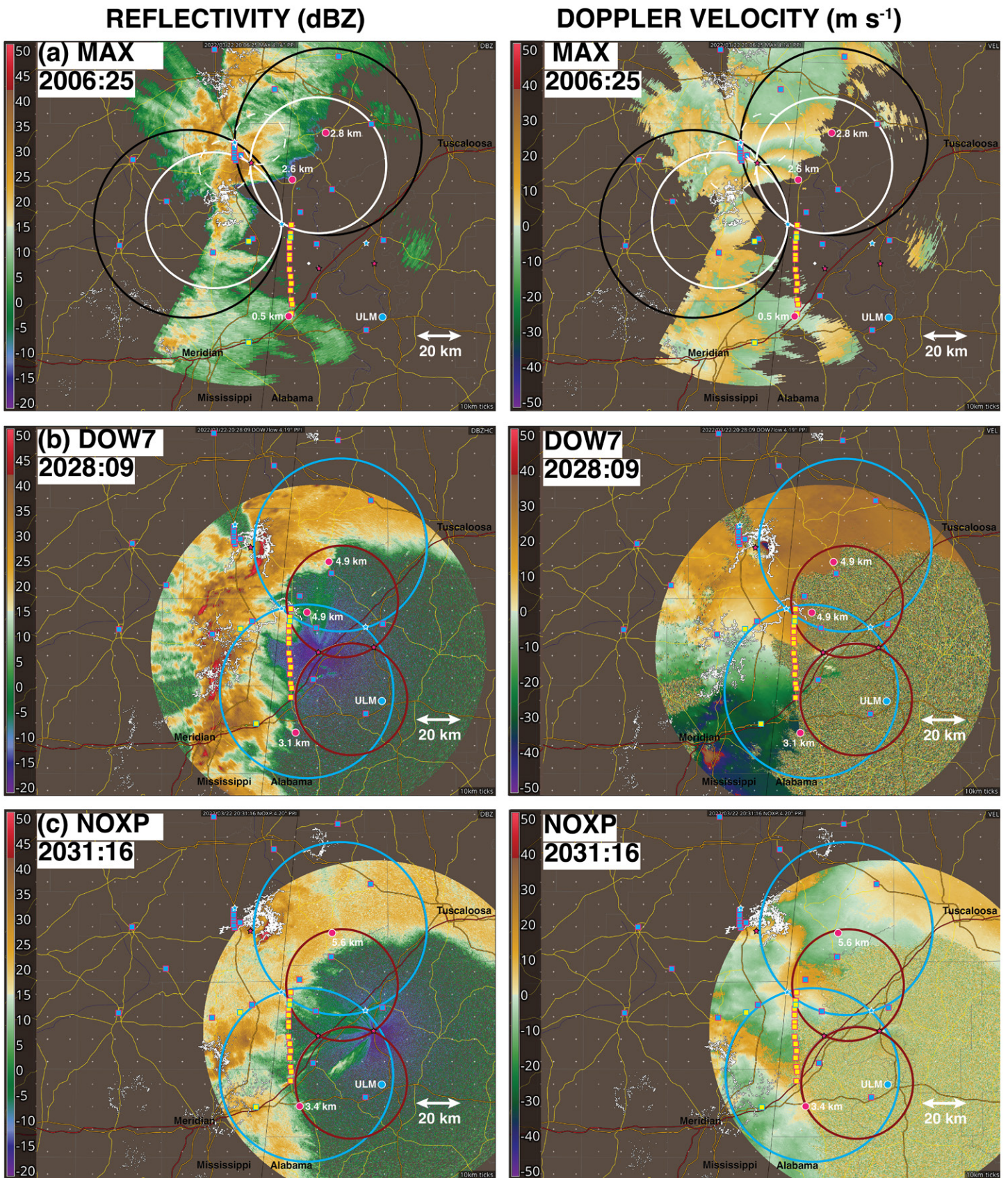


FIG. 7. As in Fig. 6, but with X-band radar data. X-band radar data are shown from (a) MAX, (b) DOW7, and (c) NOXP. The 30°-dual-Doppler lobes between SR-1 and MAX are shown in white; 30°-dual-Doppler lobes between DOW7 and NOXP are shown in crimson. The Nyquist velocities are 10 m s⁻¹ for MAX, 40 m s⁻¹ for DOW7, and 16 m s⁻¹ for NOXP.

c. Logistics. Unlike projects such as VORTEX2, PECAN, and RELAMPAGO, most teams and instruments did not reside in the field, but remained on standby at their home institutions. The resulting logistical need for longer forecast lead times resulted in unique challenges compared to adaptable-network, field-resident, projects such as VORTEX2, PECAN, or RELAMPAGO. Longer lead times imposed pressure to generate accurate 48–72-h forecasts. Also, the nonchasing deployment mode where many instruments were deployed >24 h before events meant that last-minute corrections/adaptions to the established “playbook” deployments were very constrained.

Daily forecast briefings were held virtually at 1200 U.S. Central Time and consisted of a forecast briefing and discussion, which was open to all participants, and then a rotating closed decision team (comprising four experienced participants) meeting to decide on project actions (e.g., IOP go/no go, which subdomain for operations, start time of IOP). Since teams and many of the instruments needed to travel to each IOP location from afar, IOP go/no-go decisions were made no less than 72 h in advance of the projected IOP start time (T₀). At T₀–48 (±6) h, a subdomain was selected from the 10 possible choices. At T₀–45 (±3) h, a radar configuration was picked, which then triggered other instrument teams to either design their network (e.g., profiles and soundings), begin setting up large instrument arrays (StickNet and LMA), or set up the deployable COW radar. While choosing small spatial and temporal windows for operations and executing go/no-go decisions outside the window of most CAMs were especially challenging compared to convection-studying projects with shorter lead times (e.g., PECAN and VORTEX2), the success rate during PERiLS proved very high.

4. Preliminary results and summary

PERiLS conducted four IOPs during year 1 and five IOPs during year 2. Since PERiLS crew/instrument basing was mostly remote from the operational domain, the threshold for calling an IOP was high and potentially resulted in fewer IOPs compared to fully in-field-based projects. Of the nine IOPs, seven had tornadoes within the observational array (Fig. 5). Several of the observed tornadoes were associated with supercell structures ahead of convective lines (Table 1). Three IOPs were nocturnal (T₀ after dark or predawn). Data collected during the PERiLS field phases are being used to address many of the multifaceted objectives related

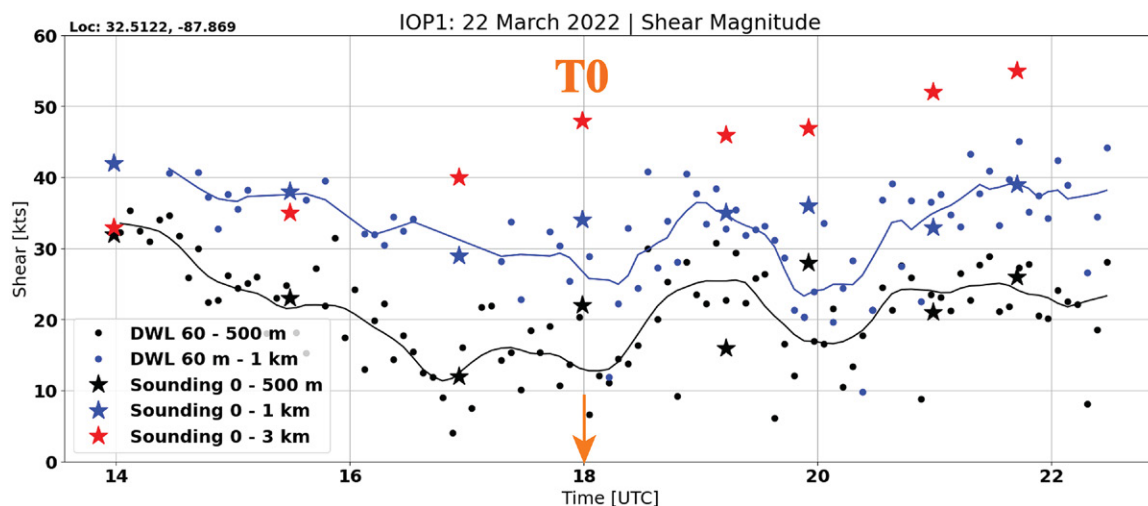


FIG. 8. Time series of bulk shear at the ULM location in Demopolis, Alabama, from the ULM DWL and ULM radiosonde launches. DWL-derived bulk shear within the 500-m layer; black dots are the 5-min observations; black line is the nonparametric smoothing function. DWL-derived bulk shear within the 1-km layer; blue dots are the 5-min observations; blue line is the nonparametric smoothing function. Stars depict the radiosonde layer shear. The correlation coefficient r between the 500-m (1 km) shear layer is 0.53 (0.62). T₀ is 1800 UTC.

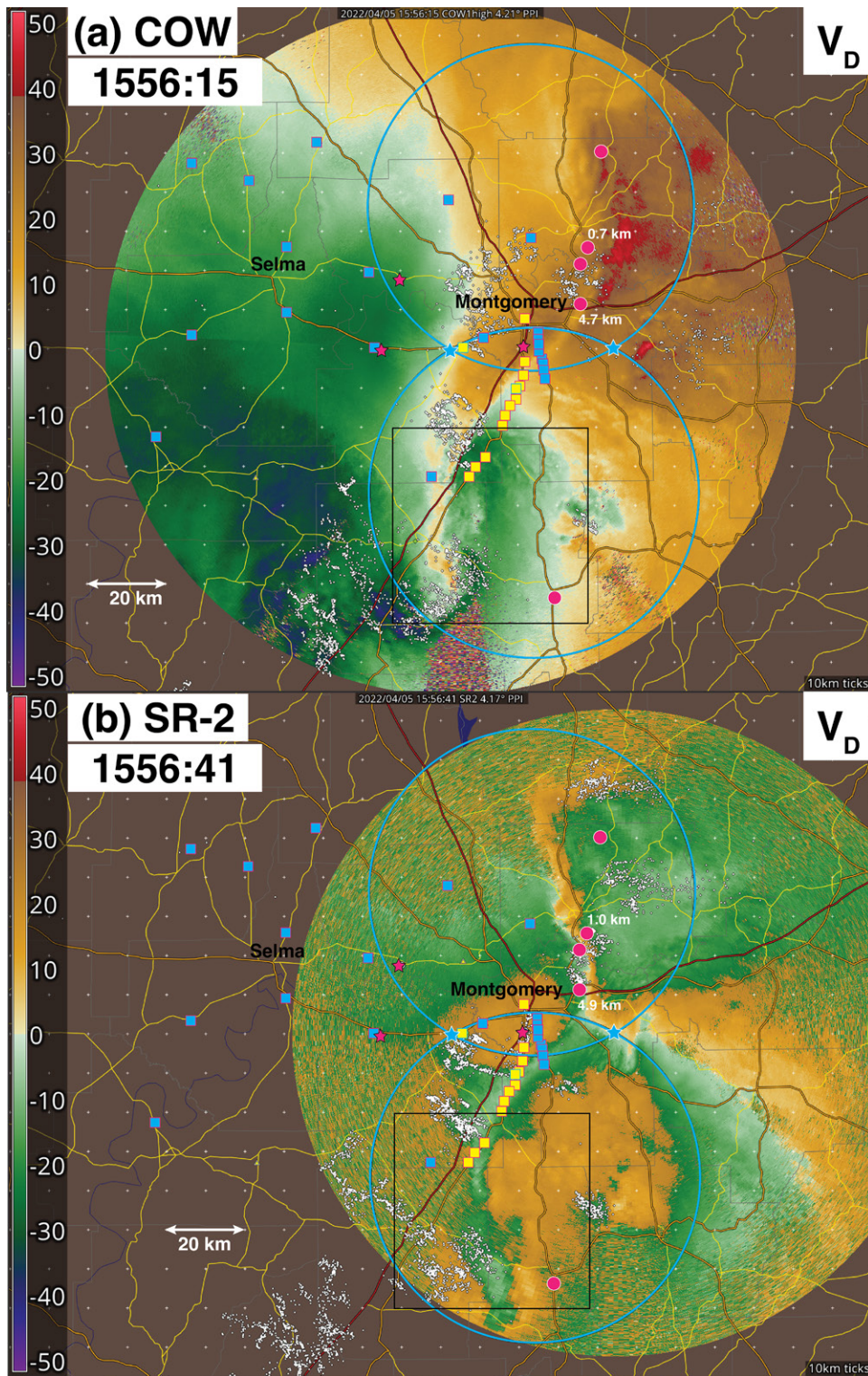


FIG. 9. Year 1, IOP3 actual deployment with select assets at about 1556 UTC 5 Apr 2022. C-band radar Doppler velocity data are shown from (a) COW and (b) SR-2 at the 4° elevation angle, which is completely unblocked for both radars. The 30° dual-Doppler lobes between COW and SR-2 are shown in blue. C-band locations are depicted with blue stars, and X-band locations are shown with pink stars. Surface assets are depicted with rectangles; yellow with pink outlines are pods; yellow with blue outlines are mesonets; blue with pink outlines are Sticks. Soundings are shown with pink circles; altitude of the sounding at that location is already launched. The white circles are total lightning from the LMA within 7 s of the radar data. The black boxes indicate the location of the dual-Doppler domain shown in Fig. 10b. The Nyquist velocities are 24 m s^{-1} for SR-2 and 68 m s^{-1} for the COW.

to QLCS tornadogenesis. Some preliminary data and findings, illustrative of the range of datasets collected, are presented below.

a. Year 1, IOP1: 22 March 2022. An example of PERiLS IOP was the first of the experiment, on 22 March 2022. The QLCS was the prototypical event that PERiLS endeavored to observe. A QLCS moved through the Brooksville domain at ~ 2000 UTC (Figs. 6 and 7 and in the online supplemental material). Several tornado warnings were issued, the PERiLS radars observed various circulations, and postevent damage surveys confirmed the occurrence of tornadoes in the PERiLS domain (Fig. 5). The southern radar array was configured to have the X-band radars cover the C-band baselines, and due to site suitability, the northern part of the radar array had fine-spatial-scale C–X-band lobes, allowing for greater spatial resolution of smaller features. The QLCS passed through the multiple-Doppler coverage area of the array (Fig. 3b), and multiple circulations, some associated with tornadoes, were documented. Preliminary local environmental data from the University of Louisiana Monroe (ULM) DWL and soundings generally showed a collapse of the low-level shear through mid-morning owing to mixing and the afternoon lull in the low-level jet (Fig. 8). Then, just after 2000 UTC, a marked increase in the 0–1-km shear began in the lead up to convection approaching PERiLS assets (Fig. 8). This increase in low-level shear is observed in several of the IOPs (e.g., section 4c), and causes for this increase are being investigated.

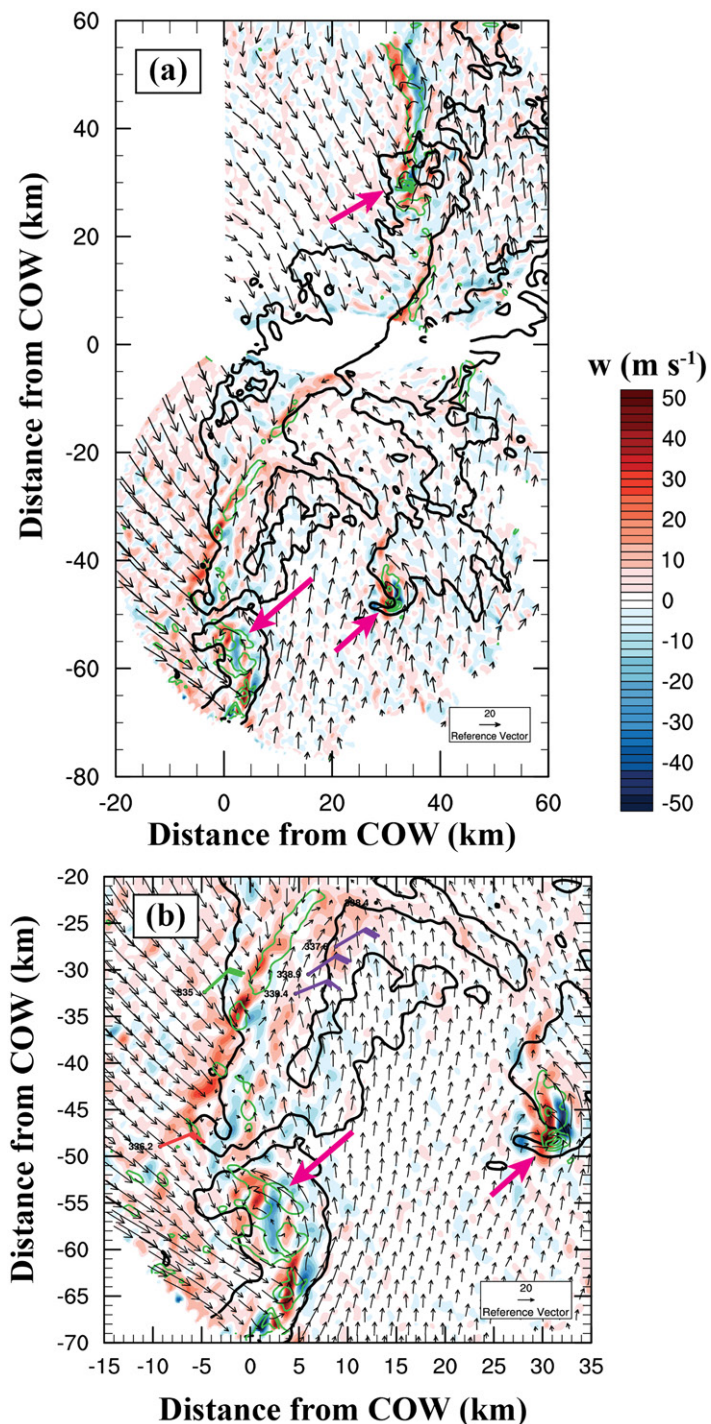


FIG. 10. Dual-Doppler analysis at 1.5 km ARL at 1556 UTC for year 1, IOP3. (a) Dual-Doppler analysis in both the northern and southern lobes using a 30° crossing angle with the COW and SR-2 radars. The black line contour is the 38-dBZ line, the green line contours are vertical vorticity starting at 0.01 in 0.02 s^{-1} increments, and the color contours are vertical velocity (m s^{-1}). (b) Select surface assets are plotted within a subsection of the southern dual-Doppler lobe (black boxes in Fig. 9). Equivalent potential temperature (numbers; K) and wind observations (barbs; m s^{-1}) from Pods (purple), Sticks (green), and MMs (orange) within the dual-Doppler domain are shown. In both (a) and (b), the winds are QLCS relative and pink arrows indicate locations of mesoscale vortices.

b. Year 1, IOP3: 5 April 2022. The third IOP in year 1 was another representative case, with the passage of a QLCS and supercells through the Selma subdomain early morning on 5 April 2022 (Fig. 9 and supplemental material). In addition to the supercells, rotation was observed along the QLCS, over a distance of ~ 100 km, revealing the potential simultaneous tornado threat from both modes. Although rotation was observed along the QLCS, only the northern vortex was associated with a tornado. A proximate sounding, launched at 1604 UTC, revealed CAPE values less than 500 J kg^{-1} and 0–6-km shear of 40 m s^{-1} , characteristic of a HSLC environment (Sherburn and Parker 2014). Only modest temperature deficits ($\sim 2 \text{ K}$) were associated with the cold pool, which might be expected given the almost saturated local environmental sounding. Prior to the existence of vortices, HSI was evaluated across the line using the methods described in Kosiba et al. (2019). Instability criteria were met, but further evaluation of the prevalence of HSI in the lead up to tornadic vortices as well as whether it is necessary versus sufficient is needed.

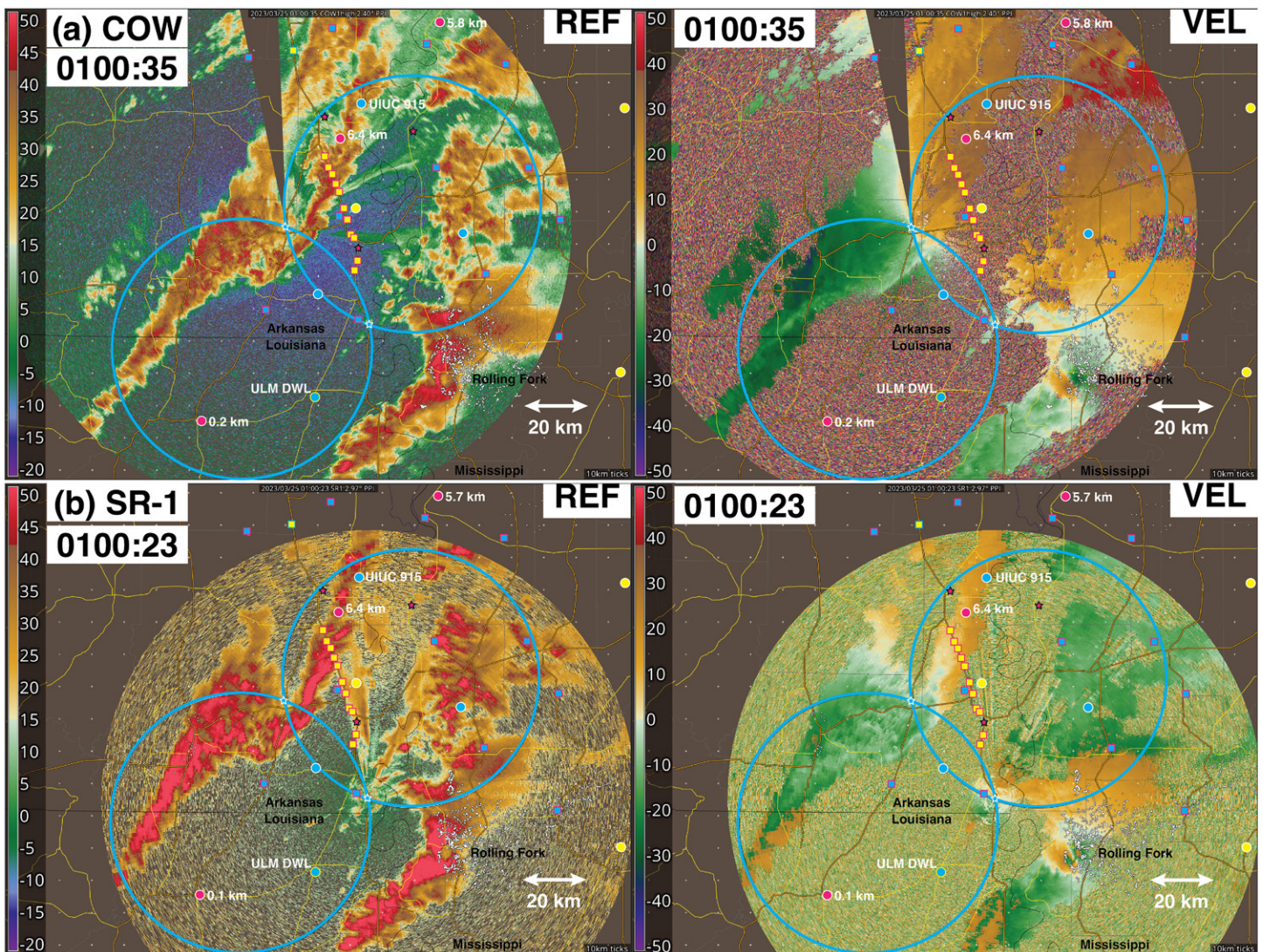


FIG. 11. Year 2, IOP3 actual deployment with select assets at about 0100 UTC 25 Mar 2023. (left) C-band radar reflectivity and (right) Doppler velocity data are shown from (a) COW and (b) SR-1. The 30° -dual-Doppler lobes between COW and SR-1 are shown in blue. C-band locations are depicted with blue stars, and X-band locations are shown with pink stars. Surface assets are depicted with rectangles; yellow with pink outlines are pods; yellow with blue outlines are mesonets; blue with pink outlines are Sticks. Profilers are shown with blue circles; CopterSonde launch locations are shown with yellow circles; soundings are shown with pink circles; altitude of the sounding at that location is given. The white circles are total lightning from the LMA within 7 s of the radar data. The Nyquist velocities are 68 m s^{-1} for the COW and 24 m s^{-1} for SR-2.

Using a 30°-minimum beam crossing angle, dual-Doppler analyses between SR-2 and the COW were conducted for IOP3 at consecutive times. Edited radar data were objectively analyzed to a Cartesian grid with horizontal grid spacing of 250 m using a two-pass Barnes scheme with a second-pass convergence parameter of 0.3. The dual-Doppler analyses were conducted using the methodology described in Kosiba et al. (2013). At 1.5 km, vertical vorticity of at least 0.01 s^{-1} was analyzed along the QLCS (Fig. 10), an order of magnitude larger than the analyses of Conrad and Knupp (2019), likely highlighting the importance of spatial resolution of the data as opposed to differences in rotation strength between the two events. The stronger vortices were associated with an updraft/downdraft couplet, suggesting that proximal downdrafts may play a role in vortex development and/or evolution. Multicase dual-Doppler analyses are underway that examine the draft characteristics over a range of vortices observed during PERiLS and VSE.

While the QLCS was exemplary, the far-eastern end of the Selma, Alabama, observational subdomain, where the meteorology necessitated the deployment, was more logistically challenging than anticipated for many of the instruments due to largely forested terrain and the paucity of presurveyed sites for radars, LMA, and StickNet. Despite these challenges, single-radar observations of rotations and dual-polarimetric signatures, combined with 1 km and above multi-Doppler, surface and LMA data, and local environmental and cold pool soundings, make this a compelling case to examine the role of HSI in mesovortex generation, cold pool properties and gust front evolution, updraft/downdraft structure, and the evolution of local environmental heterogeneities on rotation development and intensity.

c. Year 2, IOP3: 24 March 2023. In year 2, similar storm morphologies were observed and, as with year 1, will likely serve as the basis for individual case studies, as well as provide data for bulk characteristics of southeastern QLCSs and their local environment. During year 2, a notable tornado event occurred near the PERiLS operational domain during IOP3 (24 March 2023). While PERiLS established multiple-Doppler, LMA, and StickNet arrays in eastern

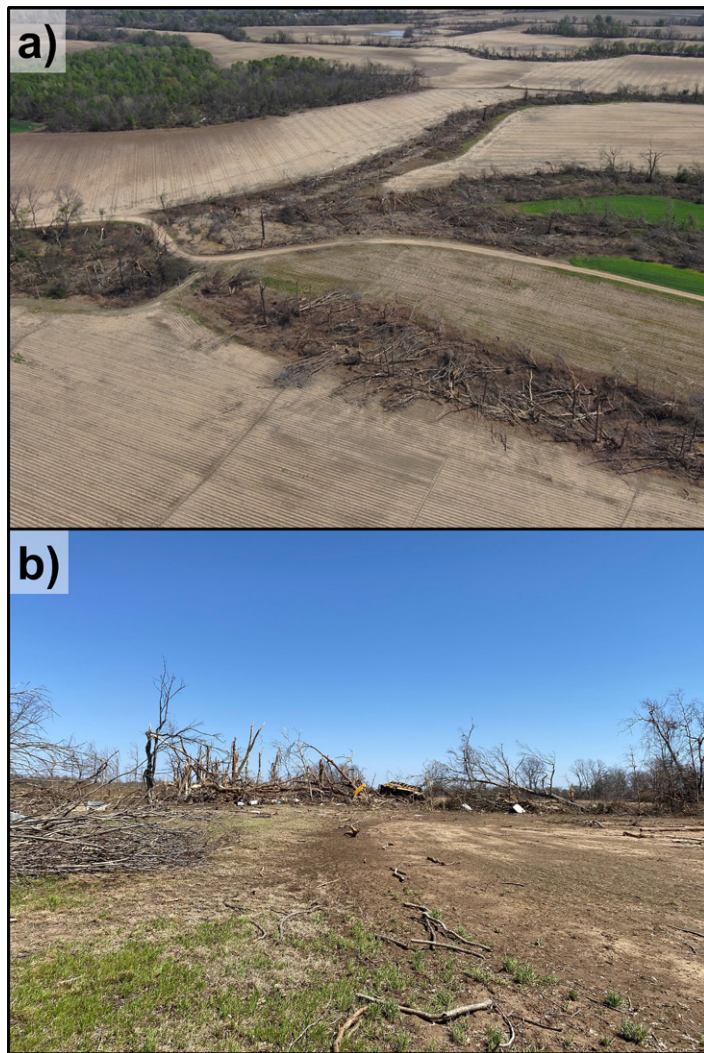


FIG. 12. Examples of damage from the 24 Mar 2023 Rolling Fork, Mississippi, tornado, observed during PERiLS year 2, IOP3. (a) High-resolution imagery from the NSSL/CIWRO multi-rotor UAS platform of damage along Widow Bayou northeast of Rolling Fork. (b) Image from the NSSL/CIWRO ground survey crew of damage along Dogwood Road, northeast of Widow Bayou. Damage in both locations was determined to be EF4 intensity by NSSL/CIWRO and NWS Jackson survey crews.

Arkansas (Fig. 11; supplemental material), in the hope of targeting a potentially tornadic QLCS, a supercellular thunderstorm formed downstream of the more linear convection and spawned an EF4-rated tornado, which caused 17 fatalities in and near Rolling Fork, Mississippi (Jackson, Mississippi, NOAA/National Weather Service 2023). This tornado was observed by some of the PERiLS radars, and PERiLS teams documented EF4 damage (Fig. 12). Polarimetric tornado debris signatures (Ryzhkov et al. 2005) were observed at ~600–700 m ARL height by the distant C-band radars (Fig. 13). The local preconvective environment was sampled by soundings, profilers (Figs. 14 and 15), and CopterSondes (Fig. 14). Preliminary data from the ULM DWL suggest that between 2200 and 2300 UTC the mid-level cap/remnant elevated mixed layer finally eroded away, surface moisture increased, and the low-level wind speeds strengthened considerably (Fig. 15). The Rolling Fork tornado occurred just before 0100 UTC. While not addressing QLCS-focused PERiLS objectives/hypotheses related to mesovortex formation, this is a compelling dataset to address scientific objectives related to differences in local environments and evolution of storm mode. The increase in low-level shear prior to vortexgenesis has been documented in several cases, and the mechanisms through which this occurs are under investigation.

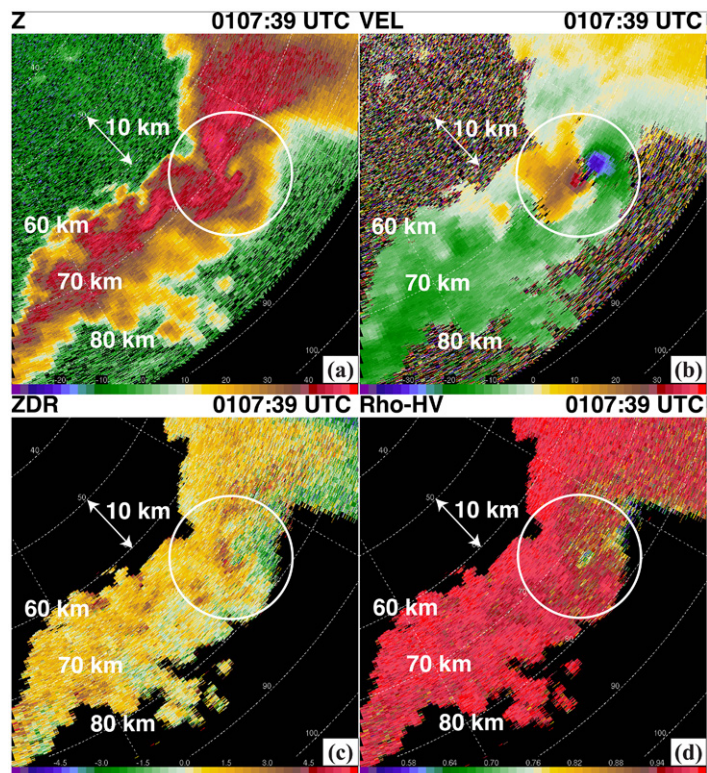


FIG. 13. The Rolling Fork, Mississippi, tornado as observed by the UIUC COW radar at 73-km range. The approximate observation height at the location of the tornado was 690 m ARL. (a) Radar reflectivity, (b) Doppler velocity, (c) differential reflectivity, and (d) cross-correlation coefficient.

d. Climatological analyses. While in-depth studies of individual cases are valuable, analyses are underway to understand bulk characteristics of QLCSs and their local environments, providing context for individual events. Examination of all the mesovortices observed by the COW during year 1 revealed that tornadic mesovortices may have a smaller diameter than nontornadic mesovortices (Fig. 16). More work is underway to determine the robustness of this finding, but a discriminator between tornadic and nontornadic mesovortices has the potential to aid forecasters. This will be particularly critical given Blind-Doskocil's (2023) additional finding that tornado-warned (and WSR-88D identified) mesovortices (MVs) have relatively weak 1-m winds, based on Pod data. Wolff (2023) used confirmed tornado locations from PERiLS storm surveys, in addition to Multi-Radar Multi-Sensor (MRMS) system 3D mosaic reflectivity products and *GOES-16* satellite data during IOP2 in year 1 to address the hypothesis that tornadic circulations are more likely to be associated with discrete deep updrafts and overshooting convection. Wolff (2023) found that all tornadoes were collocated with upper-tropospheric (9 km AGL) reflectivity cores, which were present tens of minutes prior to tornadogenesis and also prior to the identification of MVs in WSR-88D data (Fig. 17). This finding has the potential to aid forecasters in identifying possible future locations of tornadogenesis.

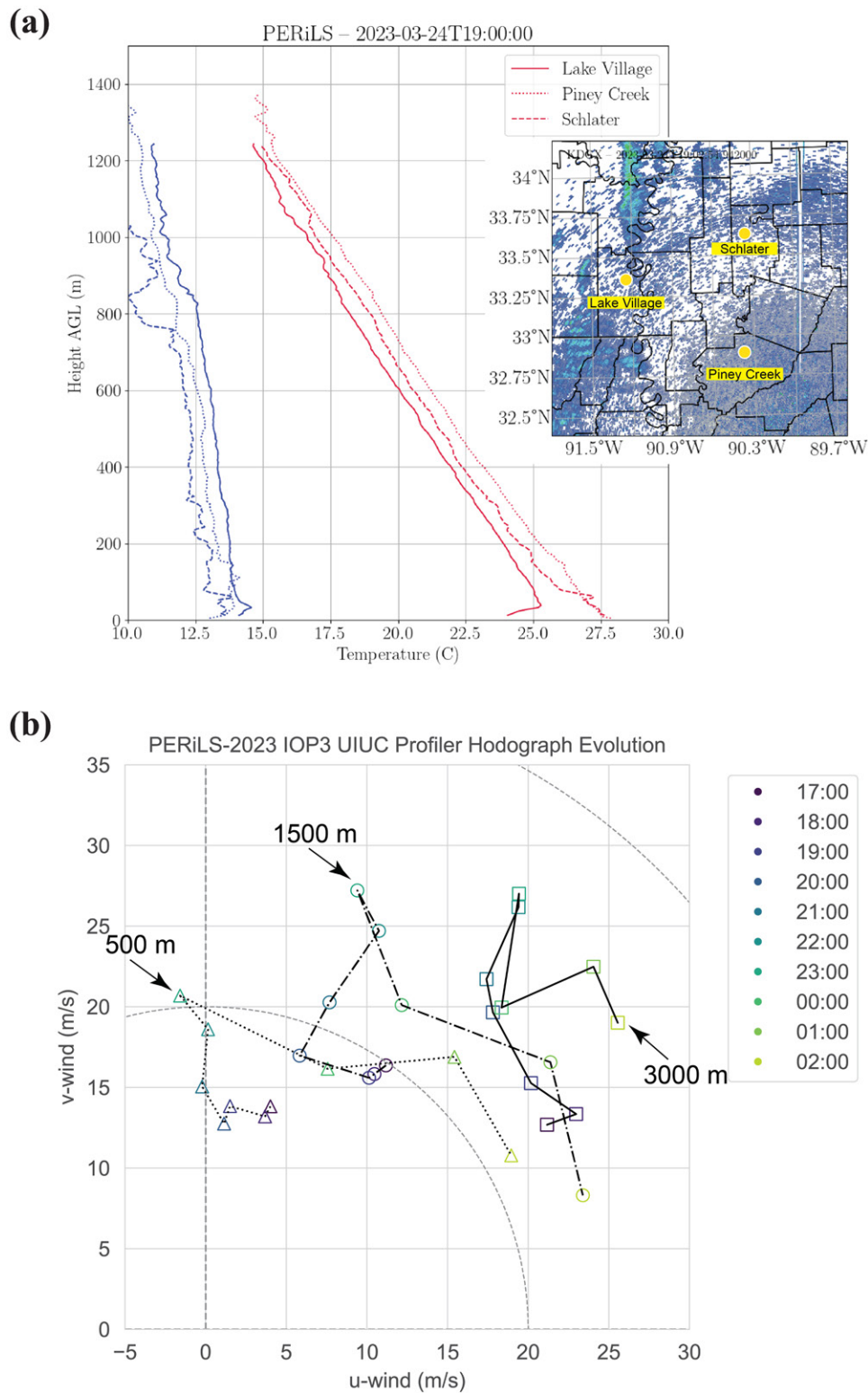


FIG. 14. Environmental data from the (a) CopterSonde and (b) UIUC 915-MHz profiler. Locations of instruments are shown in Fig. 11. (a) Temperature ($^{\circ}\text{C}$) (red) and dewpoint temperature ($^{\circ}\text{C}$) (blue) are shown as a function of height (m). (b) The wind data (m s^{-1}) in hodograph form at 500 m (dotted line), 1500 m (dashed line), and 3000 m (solid line) for various times (colored icons).

Silcott et al. (2023) have done a preliminary analysis of cold pool properties with a focus on the heterogeneity and temporal variability of cold pools across short-time and spatial scales. Using Pod, StickNet, and sounding data, Silcott et al.'s (2023) preliminary analyses revealed several AGLe general conclusions about the PERiLS cold pools. On average, the cold pools observed in year 1 exhibited a temperature drop of approximately 6 K, a decrease in

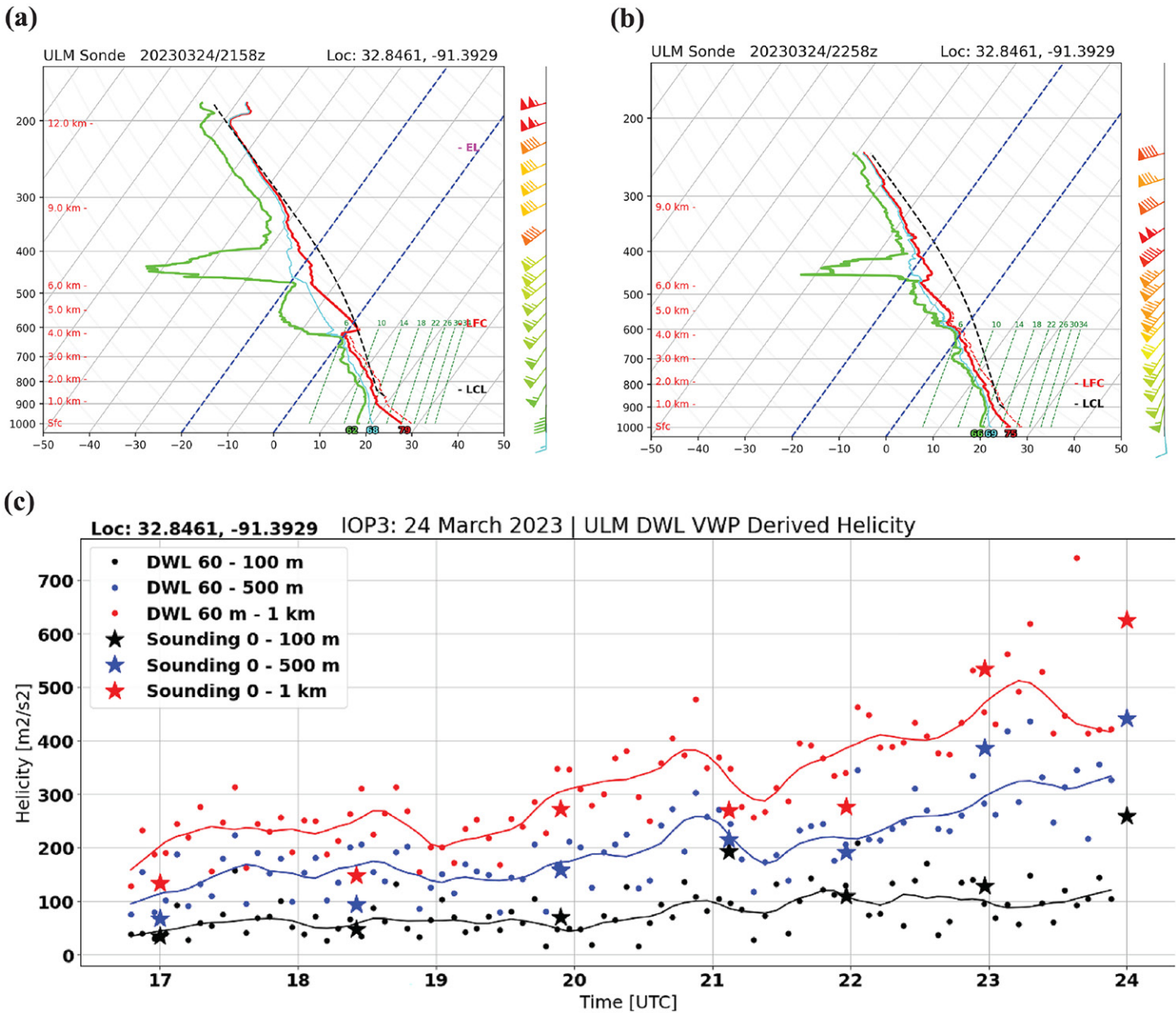


FIG. 15. ULM sounding data plotted on a skew T -log p diagram at (a) 2158 and (b) 2258 UTC and (c) time series of ULM DWL-derived helicity (dots) and sonde-derived helicity (stars). The location of the collocated sounding launch and ULM DWL is shown in Fig. 11. The correlation coefficients r between the 100-m, 500-m, and 1-km shear layers are 0.80, 0.98, and 0.88, respectively.

dewpoint temperature of around 3 K, an increase in pressure of about 3 hPa, and a wind shift of approximately 7 m s^{-1} . Additionally, the theoretical density current speed of the cold pools was approximately 13 m s^{-1} , with a corresponding cold pool depth of around 2000 m (Fig. 18). All of the cold pools would be considered rather weak in the context of those studied in higher-CAPE midlatitude large-scale environments, typically being both warmer and shallower than those studied by Engerer et al. (2008) and Bryan and Parker (2010). This finding has potential implications for the roles of cold pools in system maintenance as well as baroclinic generation of horizontal vorticity in the SE QLCSs, which may in turn modulate the associated tornado threat.

A companion longitudinal study investigating the association of mesovortex and tornado occurrence with the temperature deficits within, and gradients along the leading edge of, PERiLS cold pools is ongoing (Ostaszewski et al. 2023). These analyses indicate larger virtual potential temperature gradients are more commonly found in the vicinity of QLCS mesovortices, consistent with the many potential baroclinic controls of vorticity generation

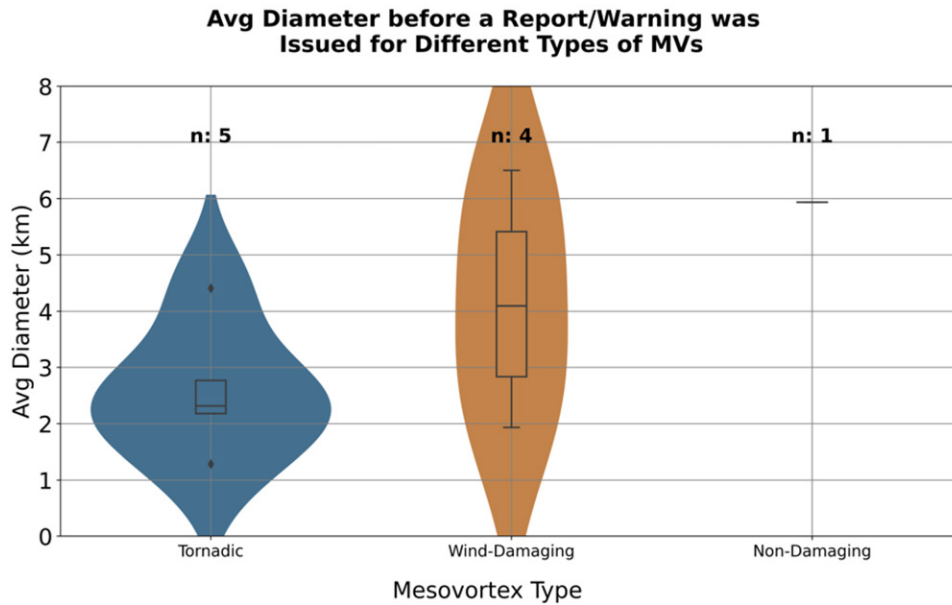


FIG. 16. Violin/box-and-whisker plots of average diameter before a report/warning was issued for 10 QLCS MVs [five tornadic (TOR), four wind damaging (WD), and one nondamaging (ND)] observed by the COW at any range of PERiLS 2022. Adapted from Blind-Doskocil (2023).

developed in previous studies. The association of these gradients with tornado occurrence is more nuanced and statistically significant for specific periods of time and distances relative to the tornado.

Scientists and students continue to analyze the rich datasets, anticipating exciting advances in our knowledge of the processes involved with the genesis and evolution of QLCS tornadoes.

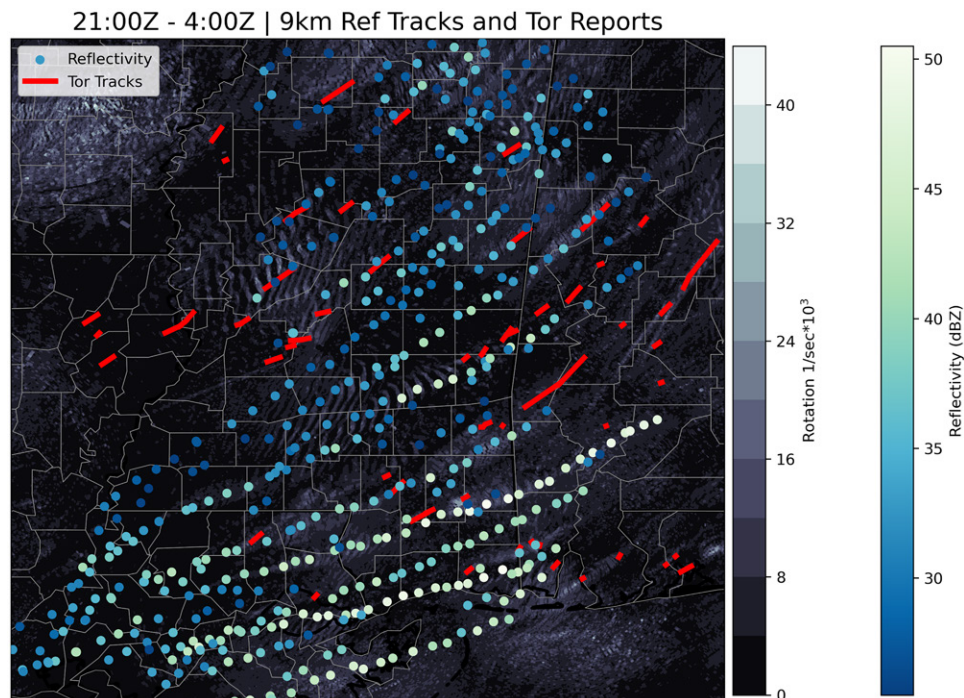


FIG. 17. Plot of MRMS 9-km constant height reflectivity cores where the marker color corresponds to the maximum reflectivity value; NCEI tornado paths are plotted in red, and MRMS low-level rotation swaths are plotted in the background. Adapted from Wolff (2023).

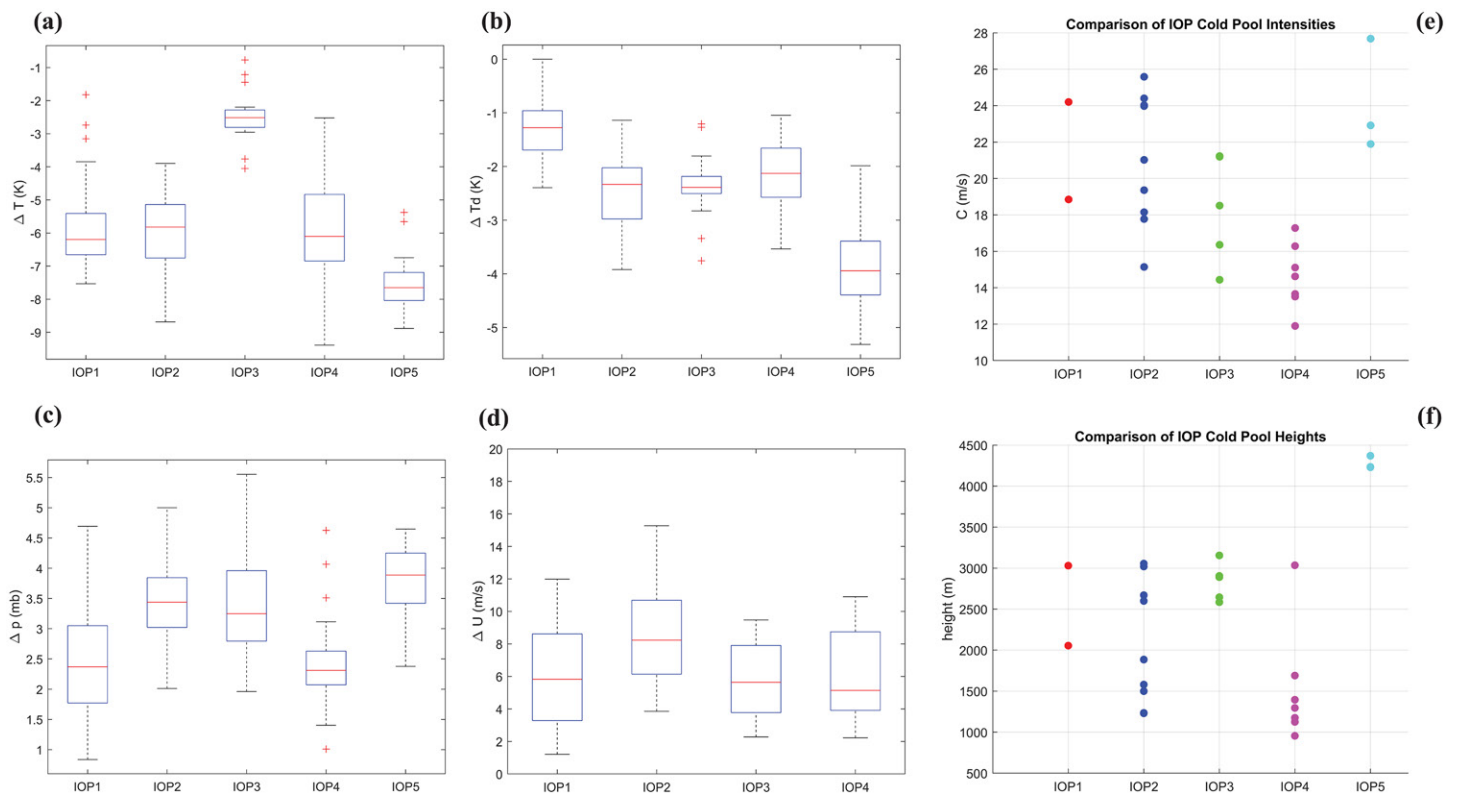


FIG. 18. Six panels depicting the distributions of cold pool characteristics across all four year 1 IOPs and year 2 IOP5. (a)–(d) The box-and-whisker plots present data collected from PERiLS surface instruments (the fine-scale pod array and StickNets). These plots display various changes across the gust front, including (a) ΔT , (b) ΔTd , (c) Δp , and (d) ΔU [with (d) only showing values for year 1]. (e),(f) The scatterplots present data from PERiLS cold pool soundings, with cold pool buoyancy, height, and intensities having been computed relative to an averaged pre-gust front sounding. (e) The theoretical cold pool speed (m s^{-1}) obtained by vertically integrating buoyancy and (f) the corresponding cold pool depths (m). Adapted from Silcott et al. (2023).

Acknowledgments. PERiLS was supported by NSF Grants AGS-2020462 and AGS-2113207 and NOAA’s VORTEX-USA program, including Grants NA21OAR4590151, NA21OAR4590323, and NA21OAR4590324, and under NOAA–University of Oklahoma Cooperative Agreement NA21OAR4320204, U.S. Department of Commerce. The PERiLS field campaign was a collaborative effort among scientists, engineers, technicians, students, administrators, and forecasters. The National Science Foundation and the National Oceanographic and Atmospheric Administration provided major support for PERiLS and for the preparation of this manuscript. The statements, findings, conclusions, and recommendations are those of the authors and do not necessarily reflect the views of NOAA or the U.S. Department of Commerce.

Data availability statement. Data are available from Wurman and Kosiba (2022a,b, 2023b) at https://data.eol.ucar.edu/master_lists/generated/perils_2022/, https://data.eol.ucar.edu/master_lists/generated/perils_2023/, and <https://www.ncei.noaa.gov/access>.

APPENDIX PERiLS Instrumentation

Table A1 shows scientific objectives, as described in section 2, addressed by each instrument or set of instruments.

TABLE A1. List of instruments fielded during PERiLS, operating institution, brief description of the instruments, and the scientific objective instruments.

| Instrument | Operating institution | Description | Objectives |
|--|--|--|----------------|
| SMART-R1 | The University of Oklahoma (OU) | 1.5° beamwidth | 2a, 2b, 2c, 2d |
| SMART-R2 (2022 only) | | C band, dual polarization | |
| COW | University of Illinois Urbana–Champaign (UIUC) the Flexible Array of Radars and Mesonets (FARM) | 1° beamwidth C band, dual polarization, dual frequency | 2a, 2b, 2c, 2d |
| DOW7 | UIUC FARM | 0.9° beamwidth | 2a, 2b, 2c, 2d |
| DOW6 | | X band, dual polarization, dual frequency | |
| NOXP | NOAA National Severe Storms Laboratory (NSSL) | 0.9° beamwidth X band, dual polarization | 2a, 2b, 2c, 2d |
| MAX | University of Alabama in Huntsville (UAH) | 0.9° beamwidth X band, dual polarization | 2a, 2b, 2c, 2d |
| DOW8 | UIUC FARM | 0.9° beamwidth X band, single polarization | 2a, 2b, 2c, 2d |
| Skylar (2023 only) | State University of New York, Stonybrook (SBU) | 2° beamwidth X band, phased array, dual polarization | 2b |
| RaXPol (2023 only) | OU | 1° beamwidth X band, dual polarization, rapid scan | 2b |
| StickNet (24) | Texas Tech University (TTU) | 2-m wind, T, RH, P; tripods | 2a, 2b, 2c, 2d |
| Pods (12) | UIUC FARM | 1-m wind, T, RH, P; hardened for in situ tornado measurements | 2a, 2b, 2c, 2d |
| Poles (1) | UIUC FARM | 4–5-m wind, T, RH, deployable on local infrastructure | 2a, 2b, 2c, 2d |
| Mobile Mesonet | UIUC FARM (3), NSSL (2), and UAH (1) | 3-m wind, T, RH, P; vehicle mounted | 2a, 2b, 2c, 2d |
| Soundings | UIUC FARM/North Carolina State University (NCSSU) (5), NSSL (2), University of Louisiana Monroe (ULM) (1), and UAH (2) | Upsonde systems (Graw, iMet, and Vaisala) | 2a, 2b, 2c, 2d |
| SwarmSondes | 2 (NSSL), 1 (SBU), 1 (UAH), and 1 Pennsylvania State University (PSU) | Lagrangian drifter systems (Windsond) | 2a, 2b, 2c, 2d |
| Disdrometers | 3 (UIUC), 6 (Purdue), and 2 (UAH) | OTT Parsivel ² optical disdrometers | 2a, 2b, 2d |
| Lidar (3) | 1 (NSSL), 1 (UAH), and 1 (ULM) | Three truck mounted | 2c |
| 915-MHz profilers (8) | UAH (2), UIUC (1), NOAA Physical Science Laboratory (PSL) (5) | 10° beamwidth UAH and UIUC mobile, PSL fixed site | 2c |
| LMA (8) | NSSL (7), TTU (1) | Total lightning, deployable sensors | 2a, 2b, 2d |
| CopterSondes | NSSL (3) | Airborne T, RH, P | 2c |
| CLAMPS | OU/NSSL (2) | Fixed site with lidar, AERI, microwave profiling radiometer, surface instruments | 2c |
| 449-MHz profiler | PSL (1) | Courtland fixed site | 2c |
| ASSIST | PSL (2) | Courtland and Columbia fixed sites | 2c |
| Microwave radiometers | PSL (2), UAH (3) | Courtland and Columbia fixed sites, mobile platforms | 2c |
| Ceilmeters | PSL (2), UAH (2) | Courtland and Columbia fixed sites, mobile platforms | 2c |
| Multirotor UAS copter | NSSL/Cooperative Institute for Severe and High-Impact Weather Research and Operations (CIWRO) | Quadcopter equipped with 4-K high-resolution visible camera | 2b |
| Fixed-wing Unmanned Aerial Systems (UAS) | NSSL/CIWRO | Fixed wing equipped with high-resolution visible and multispectral cameras | 2b |

References

- Anderson-Frey, A. K., and H. Brooks, 2019: Tornado fatalities: An environmental perspective. *Wea. Forecasting*, **34**, 1999–2015, <https://doi.org/10.1175/WAF-D-19-0119.1>.
- , Y. P. Richardson, A. R. Dean, R. L. Thompson, and B. T. Smith, 2016: Investigation of near-storm environments for tornado events and warnings. *Wea. Forecasting*, **31**, 1771–1790, <https://doi.org/10.1175/WAF-D-16-0046.1>.
- Asefi-Najafabady, S., K. Knupp, J. R. Mecikalski, R. M. Welch, and D. Phillips, 2010: Ground-based measurements and dual-Doppler analysis of 3-D wind fields and atmospheric circulations induced by a meso- γ -scale inland lake. *J. Geophys. Res.*, **115**, D23117, <https://doi.org/10.1029/2010JD014022>.
- Ashley, W. S., A. J. Krmenc, and R. Schwantes, 2008: Vulnerability due to nocturnal tornadoes. *Wea. Forecasting*, **23**, 795–807, <https://doi.org/10.1175/2008WAF2222132.1>.
- , A. M. Haberlie, and J. Strohm, 2019: A climatology of quasi-linear convective systems and their hazards in the United States. *Wea. Forecasting*, **34**, 1605–1631, <https://doi.org/10.1175/WAF-D-19-0014.1>.
- Atkins, N. T., and M. St. Laurent, 2009: Bow echo mesovortices. Part II: Their genesis. *Mon. Wea. Rev.*, **137**, 1514–1532, <https://doi.org/10.1175/2008MWR2650.1>.
- , M. L. Weisman, and L. J. Wicker, 1999: The influence of preexisting boundaries on supercell evolution. *Mon. Wea. Rev.*, **127**, 2910–2927, [https://doi.org/10.1175/1520-0493\(1999\)127<2910:TIOBPO>2.0.CO;2](https://doi.org/10.1175/1520-0493(1999)127<2910:TIOBPO>2.0.CO;2).
- , J. M. Arnott, R. W. Przybylinski, R. A. Wolf, and B. D. Ketcham, 2004: Vortex structure and evolution within bow echoes. Part I: Single-Doppler and damage analysis of the 29 June 1998 derecho. *Mon. Wea. Rev.*, **132**, 2224–2242, [https://doi.org/10.1175/1520-0493\(2004\)132<2224:VSAEWS>2.0.CO;2](https://doi.org/10.1175/1520-0493(2004)132<2224:VSAEWS>2.0.CO;2).
- , C. S. Bouchard, R. W. Przybylinski, R. J. Trapp, and G. Schmocker, 2005: Damaging surface wind mechanisms within the 10 June 2003 Saint Louis bow echo during BAMEX. *Mon. Wea. Rev.*, **133**, 2275–2296, <https://doi.org/10.1175/MWR2973.1>.
- Bartos, E. A., P. M. Markowski, and Y. P. Richardson, 2022: Three-dimensional thermodynamic observations in supercell thunderstorms from swarms of balloon-borne sondes. *Mon. Wea. Rev.*, **150**, 1689–1723, <https://doi.org/10.1175/MWR-D-21-0122.1>.
- Bell, T. M., B. R. Greene, P. M. Klein, M. Carney, and P. B. Chilson, 2020: Confronting the boundary layer data gap: Evaluating new and existing methodologies of probing the lower atmosphere. *Atmos. Meas. Tech.*, **13**, 3855–3872, <https://doi.org/10.5194/amt-13-3855-2020>.
- Biggerstaff, M. I., and Coauthors, 2005: The Shared Mobile Atmospheric Research and Teaching Radar: A collaboration to enhance research and teaching. *Bull. Amer. Meteor. Soc.*, **86**, 1263–1274, <https://doi.org/10.1175/BAMS-86-9-1263>.
- Blind-Doskocil, L. N., 2023: Radar and model-based studies of mesovortices in cool season quasi-linear convective systems. M.S. thesis, Dept. of Atmospheric Sciences, University of Illinois Urbana–Champaign, 81 pp., <https://hdl.handle.net/2142/121541>.
- Brotzge, J. A., S. E. Nelson, R. L. Thompson, and B. T. Smith, 2013: Tornado probability of detection and lead time as a function of convective mode and environmental parameters. *Wea. Forecasting*, **28**, 1261–1276, <https://doi.org/10.1175/WAF-D-12-00119.1>.
- Bryan, G. H., and M. D. Parker, 2010: Observations of a squall line and its near environment using high-frequency rawinsonde launches during VORTEX2. *Mon. Wea. Rev.*, **138**, 4076–4097, <https://doi.org/10.1175/2010MWR3359.1>.
- , and H. Morrison, 2012: Sensitivity of a simulated squall line to horizontal resolution and parameterization of microphysics. *Mon. Wea. Rev.*, **140**, 202–225, <https://doi.org/10.1175/MWR-D-11-00046.1>.
- Buban, M. S., and C. L. Ziegler, 2016: The formation of small-scale atmospheric vortices via baroclinic horizontal shearing instability. *J. Atmos. Sci.*, **73**, 2085–2104, <https://doi.org/10.1175/JAS-D-14-0385.1>.
- Carbone, R. E., 1983: A severe frontal rainband. Part II: Tornado parent vortex circulation. *J. Atmos. Sci.*, **40**, 2639–2654, [https://doi.org/10.1175/1520-0469\(1983\)040<2639:ASFRPI>2.0.CO;2](https://doi.org/10.1175/1520-0469(1983)040<2639:ASFRPI>2.0.CO;2).
- Chmielewski, V. C., and E. C. Bruning, 2016: Lightning mapping array flash detection performance with variable receiver thresholds. *J. Geophys. Res. Atmos.*, **121**, 8600–8614, <https://doi.org/10.1002/2016JD025159>.
- Clark, M. R., and D. J. Parker, 2014: On the mesoscale structure of surface wind and pressure fields near tornadic and nontornadic cold fronts. *Mon. Wea. Rev.*, **142**, 3560–3585, <https://doi.org/10.1175/MWR-D-13-00395.1>.
- Coffer, B. E., and M. D. Parker, 2017: Simulated supercells in nontornadic and tornadic VORTEX2 environments. *Mon. Wea. Rev.*, **145**, 149–180, <https://doi.org/10.1175/MWR-D-16-0226.1>.
- , ———, J. M. L. Dahl, L. J. Wicker, and A. J. Clark, 2017: Volatility of tornado genesis: An ensemble of simulated nontornadic and tornadic supercells in VORTEX2 environments. *Mon. Wea. Rev.*, **145**, 4605–4625, <https://doi.org/10.1175/MWR-D-17-0152.1>.
- Conrad, D. M., and K. R. Knupp, 2019: Doppler radar observations of horizontal shearing instability in quasi-linear convective systems. *Mon. Wea. Rev.*, **147**, 1297–1318, <https://doi.org/10.1175/MWR-D-18-0257.1>.
- Davis, C., and Coauthors, 2004: The bow echo and MCV experiment: Observations and opportunities. *Bull. Amer. Meteor. Soc.*, **85**, 1075–1094, <https://doi.org/10.1175/BAMS-85-8-1075>.
- Davis, J. M., and M. D. Parker, 2014: Radar climatology of tornadic and nontornadic vortices in high-shear, low-CAPE environments in the mid-Atlantic and southeastern United States. *Wea. Forecasting*, **29**, 828–853, <https://doi.org/10.1175/WAF-D-13-00127.1>.
- Dawson, D. T., II, M. Xue, J. A. Milbrandt, and M. K. Yau, 2010: Comparison of evaporation and cold pool development between single-moment and multimoment bulk microphysics schemes in idealized simulations of tornadic thunderstorms. *Mon. Wea. Rev.*, **138**, 1152–1171, <https://doi.org/10.1175/2009MWR2956.1>.
- , II, E. R. Mansell, and M. R. Kumjian, 2015: Does wind shear cause hydrometeor size sorting? *J. Atmos. Sci.*, **72**, 340–348, <https://doi.org/10.1175/JAS-D-14-0084.1>.
- Dial, G. L., J. P. Racy, and R. L. Thompson, 2010: Short-term convective mode evolution along synoptic boundaries. *Wea. Forecasting*, **25**, 1430–1446, <https://doi.org/10.1175/2010WAF2222315.1>.
- Doviak, R. J., and D. S. Zrić, 1984: *Doppler Radar and Weather Observations*. Academic Press, 593 pp.
- Engerer, N. A., D. J. Stensrud, and M. C. Coniglio, 2008: Surface characteristics of observed cold pools. *Mon. Wea. Rev.*, **136**, 4839–4849, <https://doi.org/10.1175/2008MWR2528.1>.
- Flournoy, M. D., and M. C. Coniglio, 2019: Origins of vorticity in a simulated tornadic mesovortex observed during PECAN on 6 July 2015. *Mon. Wea. Rev.*, **147**, 107–134, <https://doi.org/10.1175/MWR-D-18-0221.1>.
- Geerts, B., and Coauthors, 2017: The 2015 plains elevated convection at night field project. *Bull. Amer. Meteor. Soc.*, **98**, 767–786, <https://doi.org/10.1175/BAMS-D-15-00257.1>.
- Gibbs, J. G., 2021: Evaluating precursor signals for QLCS tornado and higher impact straight-line wind events. *J. Oper. Meteor.*, **9**, 62–75, <https://doi.org/10.15191/nwajom.2021.0905>.
- Goodman, S. J., D. E. Buechler, P. D. Wright, and W. D. Rust, 1988: Lightning and precipitation history of a microburst producing storm. *Geophys. Res. Lett.*, **15**, 1185–1188, <https://doi.org/10.1029/GL015i011p01185>.
- Goodnight, J. S., D. A. Chehak, and R. J. Trapp, 2022: Quantification of QLCS tornado genesis, associated characteristics, and environments across a large sample. *Wea. Forecasting*, **37**, 2087–2105, <https://doi.org/10.1175/WAF-D-22-0016.1>.
- Guarriello, F., C. J. Nowotarski, and C. C. Epifanio, 2018: Effects of the low-level wind profile on outflow position and near-surface vertical vorticity in simulated supercell thunderstorms. *J. Atmos. Sci.*, **75**, 731–753, <https://doi.org/10.1175/JAS-D-17-0174.1>.
- Hobbs, P. V., and P. O. G. Persson, 1982: The mesoscale and microscale structure and organization of clouds and precipitation in midlatitude cyclones. Part V: The substructure of narrow cold-frontal rainbands. *J. Atmos. Sci.*, **39**, 280–295, [https://doi.org/10.1175/1520-0469\(1982\)039<0280:TMAMSA>2.0.CO;2](https://doi.org/10.1175/1520-0469(1982)039<0280:TMAMSA>2.0.CO;2).

- Houston, A., B. Argrow, M. Coniglio, E. Frew, E. Rasmussen, C. Weiss, and C. Ziegler, 2019: Targeted Observation by Radars and UAS of Supercells (TORUS): Summary of the 2019 field campaign. *10th European Conf. on Severe Storms*, Krakow, Poland, European Severe Storms Laboratory, 1 pp., <https://meetingorganizer.copernicus.org/ECSS2019/ECSS2019-183.pdf>.
- Houze, R. A., 2018: 100 years of research on mesoscale convective systems. *A Century of Progress in Atmospheric and Related Sciences: Celebrating the American Meteorological Society Centennial*, Meteor. Monogr., No. 59, Amer. Meteor. Soc., 17.1–17.54, <https://doi.org/10.1175/AMSMONOGRAPH5-D-18-0001.1>.
- Jackson, Mississippi, NOAA/National Weather Service, 2023: 2023 NWS Jackson/Mississippi tornado information. Accessed 18 July 2023, <https://www.weather.gov/jan/2023tornadoinfo>.
- Jewett, B. F., and R. B. Wilhelmson, 2006: The role of forcing in cell morphology and evolution within midlatitude squall lines. *Mon. Wea. Rev.*, **134**, 3714–3734, <https://doi.org/10.1175/MWR3164.1>.
- King, J. R., M. D. Parker, K. D. Sherburn, and G. M. Lackmann, 2017: Rapid evolution of cool season, low-CAPE severe thunderstorm environments. *Wea. Forecasting*, **32**, 763–779, <https://doi.org/10.1175/WAF-D-16-0141.1>.
- Knuteson, R. O., and Coauthors, 2004: Atmospheric emitted radiance interferometer. Part II: Instrument performance. *J. Atmos. Oceanic Technol.*, **21**, 1777–1789, <https://doi.org/10.1175/JTECH-1663.1>.
- Koch, S., and E. N. Rasmussen, 2016: VORTEX-SE: Program and activities. *28th Conf. on Severe Local Storms*, Portland, OR, Amer. Meteor. Soc., 3.1, <https://ams.confex.com/ams/28SLS/webprogram/Paper300782.html>.
- Kollias, P., D. J. McLaughlin, S. Frasier, M. Oue, E. Luke, and A. Sneddon, 2018: Advances and applications in low-power phased array X-band weather radars. *2018 IEEE Radar Conf. (RadarConf18)*, Oklahoma City, OK, Institute of Electrical and Electronics Engineers, 1359–1364, <https://doi.org/10.1109/RADAR.2018.8378762>.
- Koshak, W. J., and Coauthors, 2004: North Alabama Lightning Mapping Array (LMA): VHF source retrieval algorithm and error analyses. *J. Atmos. Oceanic Technol.*, **21**, 543–558, [https://doi.org/10.1175/1520-0426\(2004\)021<0543:NALMAL>2.0.CO;2](https://doi.org/10.1175/1520-0426(2004)021<0543:NALMAL>2.0.CO;2).
- , D. M. Mach, and P. M. Bitzer, 2018: Mitigating VHF lightning source retrieval errors. *J. Atmos. Oceanic Technol.*, **35**, 1033–1052, <https://doi.org/10.1175/JTECH-D-17-0041.1>.
- Kosiba, K., J. Wurman, Y. Richardson, P. Markowski, P. Robinson, and J. Marquis, 2013: Genesis of the Goshen County, Wyoming, tornado on 5 June 2009 during VORTEX2. *Mon. Wea. Rev.*, **141**, 1157–1181, <https://doi.org/10.1175/MWR-D-12-00056.1>.
- Kosiba, K. A., and J. Wurman, 2016: The TWIRL (Tornado Winds from In-situ and Radars at Low-level) project. *28th Conf. on Severe Local Storms*, Portland, OR, Amer. Meteor. Soc., 4.2, <https://ams.confex.com/ams/28SLS/webprogram/Paper302011.html>.
- , K. Knupp, K. Pennington, and P. Robinson, 2019: Ontario Winter Lake-effect Systems (OWLs): Bulk characteristics and kinematic evolution of misovortices in long-lake-axis-parallel snowbands. *Mon. Wea. Rev.*, **148**, 131–157, <https://doi.org/10.1175/MWR-D-19-0182.1>.
- Kumjian, M. R., and A. V. Ryzhkov, 2012: The impact of size sorting on the polarimetric radar variables. *J. Atmos. Sci.*, **69**, 2042–2060, <https://doi.org/10.1175/JAS-D-11-0125.1>.
- Lee, J. J., T. Samaras, and C. Young, 2004: Pressure measurements at the ground in an F-4 tornado. Preprints, *22nd Conf. on Severe Local Storms*, Hyannis, MA, Amer. Meteor. Soc., 15.3, <https://ams.confex.com/ams/11aram22sls/webprogram/Paper81700.html>.
- Liu, C., D. J. Cecil, E. J. Zipser, K. Kronfeld, and R. Robertson, 2012: Relationships between lightning flash rates and radar reflectivity vertical structures in thunderstorms over the tropics and subtropics. *J. Geophys. Res.*, **117**, D06212, <https://doi.org/10.1029/2011JD017123>.
- Löffler-Mang, M., and J. Joss, 2000: An optical disdrometer for measuring size and velocity of hydrometeors. *J. Atmos. Oceanic Technol.*, **17**, 130–139, [https://doi.org/10.1175/1520-0426\(2000\)017<0130:AODFMS>2.0.CO;2](https://doi.org/10.1175/1520-0426(2000)017<0130:AODFMS>2.0.CO;2).
- Lombardo, K., 2020: Squall line response to coastal mid-Atlantic thermodynamic heterogeneities. *J. Atmos. Sci.*, **77**, 4143–4170, <https://doi.org/10.1175/JAS-D-20-0044.1>.
- Lovell, L. T., and M. D. Parker, 2022: Simulated QLCS vortices in a high-shear low-CAPE environment. *Wea. Forecasting*, **37**, 989–1012, <https://doi.org/10.1175/WAF-D-21-0133.1>.
- Mahale, V. N., J. A. Brotzge, and H. B. Bluestein, 2012: An analysis of vortices embedded within a quasi-linear convective system using X-band polarimetric radar. *Wea. Forecasting*, **27**, 1520–1537, <https://doi.org/10.1175/WAF-D-11-00135.1>.
- Mahalik, M. C., E. N. Rasmussen, S. S. Murdzek, and S. Waugh, 2018: Analysis of radar-estimated rotation and divergence associated with kinematic features observed during RiVorS. *29th Conf. on Severe Local Storms*, Stowe, VT, Amer. Meteor. Soc., 93, <https://ams.confex.com/ams/29SLS/webprogram/Paper348677.html>.
- Markowski, P., and Y. Richardson, 2014: What we know and don't know about tornado formation. *Phys. Today*, **67**, 26–31, <https://doi.org/10.1063/PT.3.2514>.
- , and Coauthors, 2012: The pretornadic phase of the Goshen County, Wyoming, supercell of 5 June 2009 intercepted by VORTEX2. Part I: Evolution of kinematic and surface thermodynamic fields. *Mon. Wea. Rev.*, **140**, 2887–2915, <https://doi.org/10.1175/MWR-D-11-00336.1>.
- Markowski, P. M., J. M. Straka, and E. N. Rasmussen, 2002: Direct surface thermodynamic observations within the rear-flank downdrafts of nontornadic and tornadic supercells. *Mon. Wea. Rev.*, **130**, 1692–1721, [https://doi.org/10.1175/1520-0493\(2002\)130<1692:DSTOWT>2.0.CO;2](https://doi.org/10.1175/1520-0493(2002)130<1692:DSTOWT>2.0.CO;2).
- , Y. P. Richardson, S. J. Richardson, and A. Petersson, 2018: Aboveground thermodynamic observations in convective storms from balloonborne probes acting as pseudo-Lagrangian drifters. *Bull. Amer. Meteor. Soc.*, **99**, 711–724, <https://doi.org/10.1175/BAMS-D-17-0204.1>.
- Marquis, J. N., Y. P. Richardson, and J. M. Wurman, 2007: Kinematic observations of misocyclones along boundaries during IHOP. *Mon. Wea. Rev.*, **135**, 1749–1768, <https://doi.org/10.1175/MWR3367.1>.
- , K. Kosiba, J. Wurman, and P. Robinson, 2018: Characteristics of QLCS downdrafts and environments observed during the VORTEX-Southeast project. *29th Conf. on Severe Local Storms*, Stowe, VT, Amer. Meteor. Soc., 151, <https://ams.confex.com/ams/29SLS/webprogram/Paper348526.html>.
- McDonald, J. M., and C. C. Weiss, 2021: Cold pool characteristics of tornadic quasi-linear convective systems and other convective modes observed during VORTEX-SE. *Mon. Wea. Rev.*, **149**, 821–840, <https://doi.org/10.1175/MWR-D-20-0226.1>.
- Mecikalski, R. M., and L. D. Carey, 2017: Lightning characteristics relative to radar, altitude and temperature for a multicell, MCS and supercell over northern Alabama. *Atmos. Res.*, **191**, 128–140, <https://doi.org/10.1016/j.atmosres.2017.03.001>.
- Mulholland, J. P., J. Frame, S. W. Nesbitt, S. M. Steiger, K. A. Kosiba, and J. Wurman, 2017: Observations of misovortices within a long-lake-axis-parallel lake-effect snowband during the OWLeS project. *Mon. Wea. Rev.*, **145**, 3265–3291, <https://doi.org/10.1175/MWR-D-16-0430.1>.
- Murphy, T. A., T. M. Stetzer, L. Walker, T. Fricker, B. Bryant, and C. Woodrum, 2022: Analysis of the April 12, 2020 north Louisiana tornadic QLCS. *J. Oper. Meteor.*, **10**, 43–62, <https://doi.org/10.15191/nwajom.2022.1004>.
- Nesbitt, S. W., and Coauthors, 2021: A storm safari in subtropical South America: Proyecto RELAMPAGO. *Bull. Amer. Meteor. Soc.*, **102**, E1621–E1644, <https://doi.org/10.1175/BAMS-D-20-0029.1>.
- Ostaszewski, J. S., C. C. Weiss, and J. M. McDonald, 2023: Analysis of QLCS cold pool intercepts during the PERILS project. *Third Symp. on Mesoscale Processes*, Baltimore, MD, Amer. Meteor. Soc., 290, <https://ams.confex.com/ams/103ANNUAL/meetingapp.cgi/Paper/416880>.
- Palmer, R., and Coauthors, 2009: Weather radar education at the University of Oklahoma—An integrated interdisciplinary approach. *Bull. Amer. Meteor. Soc.*, **90**, 1277–1282, <https://doi.org/10.1175/2009BAMS2738.1>.
- Parker, M. D., B. S. Borchardt, R. L. Miller, and C. L. Ziegler, 2020: Simulated evolution and severe wind production by the 25–26 June 2015 nocturnal

- MCS from PECAN. *Mon. Wea. Rev.*, **148**, 183–209, <https://doi.org/10.1175/MWR-D-19-0072.1>.
- Pazmany, A. L., J. B. Mead, H. B. Bluestein, J. C. Snyder, and J. B. Houser, 2013: A mobile rapid-scanning X-band polarimetric (RaXPo) Doppler radar system. *J. Atmos. Oceanic Technol.*, **30**, 1398–1413, <https://doi.org/10.1175/JTECH-D-12-00166.1>.
- Pearson, G., F. Davies, and C. Collier, 2009: An analysis of the performance of the UFAM pulsed Doppler lidar for observing the boundary layer. *J. Atmos. Oceanic Technol.*, **26**, 240–250, <https://doi.org/10.1175/2008JTECHA1128.1>.
- Przybylinski, R. W., G. K. Schmocker, and Y.-J. Lin, 2000: A study of storm and vortex morphology during the ‘intensifying stage’ of severe wind mesoscale convective systems. Preprints, *20th Conf. on Severe Local Storms*, Orlando, FL, Amer. Meteor. Soc., 173–176.
- Rasmussen, E. N., J. M. Straka, R. Davies-Jones, C. A. Doswell III, F. H. Carr, M. D. Eilts, and D. R. MacGorman, 1994: Verification of the origins of rotation in tornadoes experiment: VORTEX. *Bull. Amer. Meteor. Soc.*, **75**, 995–1006, [https://doi.org/10.1175/1520-0477\(1994\)075<0995:VOTOOR>2.0.CO;2](https://doi.org/10.1175/1520-0477(1994)075<0995:VOTOOR>2.0.CO;2).
- Rison, W., R. J. Thomas, P. R. Krehbiel, T. Hamlin, and J. Harlin, 1999: A GPS-based three-dimensional lightning mapping system: Initial observations in central New Mexico. *Geophys. Res. Lett.*, **26**, 3573–3576, <https://doi.org/10.1029/1999GL010856>.
- Rochette, L., W. L. Smith, M. Howard, and T. Bratcher, 2009: ASSIST, Atmospheric Sounder Spectrometer for Infrared Spectral Technology: Latest development and improvement in the atmospheric sounding technology. *Proc. SPIE Int. Society for Optical Engineering*, San Diego, CA, Society of Photo-Optical Instrumentation Engineers, 745702, <https://doi.org/10.1117/12.829344>.
- Rose, T., S. Crewell, U. Löhnert, and C. Simmer, 2005: A network suitable microwave radiometer for operational monitoring of the cloudy atmosphere. *Atmos. Res.*, **75**, 183–200, <https://doi.org/10.1016/j.atmosres.2004.12.005>.
- Ryzhkov, A. V., T. J. Schuur, D. W. Burgess, and D. S. Zrnic, 2005: Polarimetric tornado detection. *J. Appl. Meteor.*, **44**, 557–570, <https://doi.org/10.1175/JAM2235.1>.
- Salinas, V., E. C. Bruning, and E. R. Mansell, 2022: Examining the kinematic structures within which lightning flashes are initiated using a cloud-resolving model. *J. Atmos. Sci.*, **79**, 513–530, <https://doi.org/10.1175/JAS-D-21-0132.1>.
- Schaumann, J. S., and R. W. Przybylinski, 2012: Operational application of 0–3 km bulk shear vectors in assessing quasi-linear convective system mesovortex and tornado potential. *26th Conf. on Severe Local Storms*, Nashville, TN, Amer. Meteor. Soc., 142, <https://ams.confex.com/ams/26SLS/webprogram/Paper212008.html>.
- Schenkman, A. D., M. Xue, and A. Shapiro, 2012: Tornadogenesis in a simulated mesovortex within a mesoscale convective system. *J. Atmos. Sci.*, **69**, 3372–3390, <https://doi.org/10.1175/JAS-D-12-038.1>.
- Schneider, R. S., and A. R. Dean, 2008: A comprehensive 5-year severe storm environment climatology for the continental United States. *24th Conf. on Severe Local Storms*, Savannah, GA, Amer. Meteor. Soc., 16A.4, https://ams.confex.com/ams/24SLS/techprogram/paper_141748.htm.
- Segales, A. R., B. R. Greene, T. M. Bell, W. Doyle, J. J. Martin, E. A. Pillar-Little, and P. B. Chilson, 2020: The CopterSonde: An insight into the development of a smart unmanned aircraft system for atmospheric boundary layer research. *Atmos. Meas. Tech.*, **13**, 2833–2848, <https://doi.org/10.5194/amt-13-2833-2020>.
- Sharma, M., R. L. Tanamachi, E. C. Bruning, and K. M. Calhoun, 2021: Polarimetric and electrical structure of the 19 May 2013 Edmond–Carney, Oklahoma, tornadic supercell. *Mon. Wea. Rev.*, **149**, 2049–2078, <https://doi.org/10.1175/MWR-D-20-0280.1>.
- Sherburn, K. D., and M. D. Parker, 2014: Climatology and ingredients of significant severe convection in high-shear, low-CAPE environments. *Wea. Forecasting*, **29**, 854–877, <https://doi.org/10.1175/WAF-D-13-00041.1>.
- , and —, 2019: The development of severe vortices within simulated high-shear, low-CAPE convection. *Mon. Wea. Rev.*, **147**, 2189–2216, <https://doi.org/10.1175/MWR-D-18-0246.1>.
- , —, J. R. King, and G. M. Lackmann, 2016: Composite environments of severe and nonsevere high-shear, low-CAPE convective events. *Wea. Forecasting*, **31**, 1899–1927, <https://doi.org/10.1175/WAF-D-16-0086.1>.
- Silcott, M. K., M. D. Parker, K. A. Kosiba, S. W. Nesbitt, R. J. Trapp, and J. Wurman, 2023: Structures of cold pools from PERiLS 2022 and 2023. *20th Conf. on Mesoscale Processes*, Madison, WI, Amer. Meteor. Soc., 23, <https://ams.confex.com/ams/WAFNWPM/meetingapp.cgi/Paper/425181>.
- Skinner, P. S., C. C. Weiss, L. J. Wicker, C. K. Potvin, and D. C. Dowell, 2015: Forcing mechanisms for an internal rear-flank downdraft momentum surge in the 18 May 2010 Dumas, Texas, supercell. *Mon. Wea. Rev.*, **143**, 4305–4330, <https://doi.org/10.1175/MWR-D-15-0164.1>.
- Smith, B. T., R. L. Thompson, J. S. Grams, C. Broyles, and H. E. Brooks, 2012: Convective modes for significant severe thunderstorms in the contiguous United States. Part I: Storm classification and climatology. *Wea. Forecasting*, **27**, 1114–1135, <https://doi.org/10.1175/WAF-D-11-00115.1>.
- Stough, S. M., L. D. Carey, C. J. Schultz, and P. M. Bitzer, 2017: Investigating the relationship between lightning and mesocyclonic rotation in supercell thunderstorms. *Wea. Forecasting*, **32**, 2237–2259, <https://doi.org/10.1175/WAF-D-17-0025.1>.
- Strader, S. M., and W. S. Ashley, 2018: Finescale assessment of mobile home tornado vulnerability in the central and southeast United States. *Wea. Climate Soc.*, **10**, 797–812, <https://doi.org/10.1175/WCAS-D-18-0060.1>.
- Thomas, R. J., P. R. Krehbiel, W. Rison, S. J. Hunyady, W. P. Winn, T. Hamlin, and J. Harlin, 2004: Accuracy of the lightning mapping array. *J. Geophys. Res.*, **109**, D14207, <https://doi.org/10.1029/2004JD004549>.
- Thompson, R. L., B. T. Smith, J. S. Grams, A. R. Dean, and C. Broyles, 2012: Convective modes for significant severe thunderstorms in the contiguous United States. Part II: Supercell and QLCS tornado environments. *Wea. Forecasting*, **27**, 1136–1154, <https://doi.org/10.1175/WAF-D-11-00116.1>.
- Tokay, A., D. B. Wolff, and W. A. Petersen, 2014: Evaluation of the new version of the laser-optical disdrometer, OTT Parsivel². *J. Atmos. Oceanic Technol.*, **31**, 1276–1288, <https://doi.org/10.1175/JTECH-D-13-00174.1>.
- Trapp, R. J., 1999: Observations of nontornadic low-level mesocyclones and attendant tornadogenesis failure during VORTEX. *Mon. Wea. Rev.*, **127**, 1693–1705, [https://doi.org/10.1175/1520-0493\(1999\)127<1693:OONLLM>2.0.CO;2](https://doi.org/10.1175/1520-0493(1999)127<1693:OONLLM>2.0.CO;2).
- , and M. L. Weisman, 2003: Low-level mesovortices within squall lines and bow echoes. Part II: Their genesis and implications. *Mon. Wea. Rev.*, **131**, 2804–2823, [https://doi.org/10.1175/1520-0493\(2003\)131<2804:LMWLSA>2.0.CO;2](https://doi.org/10.1175/1520-0493(2003)131<2804:LMWLSA>2.0.CO;2).
- , E. D. Mitchell, G. A. Tipton, D. W. Effertz, A. I. Watson, D. L. Andra Jr., and M. A. Magsig, 1999: Descending and nondescending tornadic vortex signatures detected by WSR-88Ds. *Wea. Forecasting*, **14**, 625–639, [https://doi.org/10.1175/1520-0434\(1999\)014<0625:DANTVS>2.0.CO;2](https://doi.org/10.1175/1520-0434(1999)014<0625:DANTVS>2.0.CO;2).
- , S. A. Tessendorf, E. S. Godfrey, and H. E. Brooks, 2005: Tornadoes from squall lines and bow echoes. Part I: Climatological distribution. *Wea. Forecasting*, **20**, 23–34, <https://doi.org/10.1175/WAF-835.1>.
- Turner, D., U. Löhnert, J. Gebauer, T. Bell, and G. Blumberg, 2022: TROPoe: Tropospheric Remotely Observed Profiling via optical estimation. *EGU General Assembly 2022*, Vienna, Austria, European Geosciences Union, EGU22-10512, <https://doi.org/10.5194/egusphere-egu22-10512>.
- Turner, D. D., and U. Löhnert, 2021: Ground-based temperature and humidity profiling: Combining active and passive remote sensors. *Atmos. Meas. Tech.*, **14**, 3033–3048, <https://doi.org/10.5194/amt-14-3033-2021>.
- Ungar, M. D., and M. C. Coniglio, 2023: Using radiosonde observations to assess the “three ingredients method” to forecast QLCS mesovortices. *Wea. Forecasting*, **38**, 2441–2460, <https://doi.org/10.1175/WAF-D-22-0176.1>.
- Vincent, B. R., L. Carey, D. Schneider, K. Keeter, and R. Gonski, 2003: Using WSR-88D reflectivity data for the prediction of cloud-to-ground lightning: A central North Carolina study. *Natl. Wea. Dig.*, **27**, 35–44.
- Wagner, T. J., P. M. Klein, and D. D. Turner, 2019: A new generation of ground-based mobile platforms for active and passive profiling of the boundary layer. *Bull. Amer. Meteor. Soc.*, **100**, 137–153, <https://doi.org/10.1175/BAMS-D-17-0165.1>.
- Wakimoto, R. M., H. V. Murphey, C. A. Davis, and N. T. Atkins, 2006: High winds generated by bow echoes. Part II: The relationship between the mesovortices and damaging straight-line winds. *Mon. Wea. Rev.*, **134**, 2813–2829, <https://doi.org/10.1175/MWR3216.1>.

- Weisman, M. L., and R. J. Trapp, 2003: Low-level mesovortices within squall lines and bow echoes. Part I: Overview and dependence on environmental shear. *Mon. Wea. Rev.*, **131**, 2779–2803, [https://doi.org/10.1175/1520-0493\(2003\)131<2779:LMWLSLA>2.0.CO;2](https://doi.org/10.1175/1520-0493(2003)131<2779:LMWLSLA>2.0.CO;2).
- Weiss, C. C., and J. L. Schroeder, 2008: StickNet: A new portable, rapidly deployable surface observation system. *Bull. Amer. Meteor. Soc.*, **89**, 1502–1503.
- Wheatley, D. M., and R. J. Trapp, 2008: The effect of mesoscale heterogeneity on the genesis and structure of mesovortices within quasi-linear convective systems. *Mon. Wea. Rev.*, **136**, 4220–4241, <https://doi.org/10.1175/2008MWR2294.1>.
- , ———, and N. T. Atkins, 2006: Radar and damage analysis of severe bow echoes observed during BAMEX. *Mon. Wea. Rev.*, **134**, 791–806, <https://doi.org/10.1175/MWR3100.1>.
- Williams, E., and Coauthors, 1999: The behavior of total lightning activity in severe Florida thunderstorms. *Atmos. Res.*, **51**, 245–265, [https://doi.org/10.1016/S0169-8095\(99\)00011-3](https://doi.org/10.1016/S0169-8095(99)00011-3).
- Wolff, E. C., 2023: Examining the role of deep convective updrafts in QLCS tornadogenesis using observations and real-world modeling. M.S. thesis, Dept. of Atmospheric Sciences, University of Illinois Urbana–Champaign, 78 pp., <https://hdl.handle.net/2142/121529>.
- Wu, F., and K. Lombardo, 2021: Precipitation enhancement in squall lines moving over mountainous coastal regions. *J. Atmos. Sci.*, **78**, 3089–3113, <https://doi.org/10.1175/JAS-D-20-0222.1>.
- Wurman, J., 1998: Preliminary results from the ROTATE-98 tornado experiment. *Proc. 19th Conf. on Severe Local Storms*, Minneapolis, MN, Amer. Meteor. Soc., 120–123.
- , 2003: Multiple-Doppler observations of tornadoes and tornadogenesis from the ROTATE-2003 project. *31st Int. Conf. on Radar Meteorology*, Seattle, WA, Amer. Meteor. Soc., P4A.1, <https://ams.confex.com/ams/32BC31R5C/webprogram/Paper63886.html>.
- , 2008: Preliminary results and report of the ROTATE-2008 radar/in-situ mobile mesonet experiment. *24th Conf. on Severe Local Storms*, Savannah, GA, Amer. Meteor. Soc., 5.4, https://ams.confex.com/ams/24SLS/techprogram/paper_142200.htm.
- , and K. Kosiba, 2022a: Flexible array of radars and mesonets, radar data, PERILS (version 1). Flexible Array of Radars and Mesonets, University of Illinois, accessed 1 June 2023, <https://doi.org/10.48514/BJJZ-KF06>.
- , and ———, 2022b: Flexible array of radars and mesonets, non-radar data, PERILS. Flexible Array of Radars and Mesonets, University of Illinois, accessed 1 June 2023, <https://doi.org/10.48514/962K-9866>.
- , and K. A. Kosiba, 2023a: The BEST project (Boundary-layer Evolution and Structure of Tornadoes) kinematic and thermodynamic observations of tornadoes. *40th Conf. on Radar Meteorology*, Minneapolis, MN, Amer. Meteor. Soc., 7A.6, <https://ams.confex.com/ams/40RADAR/meetingapp.cgi/Paper/426164>.
- , and K. Kosiba, 2023b: Flexible array of radars and mesonets, radar data, PERILS (version 1). Flexible Array of Radars and Mesonets, University of Illinois, accessed 1 June 2023, <https://doi.org/10.48514/K7WX-NP56>.
- , D. Dowell, Y. Richardson, P. Markowski, E. Rasmussen, D. Burgess, L. Wicker, and H. B. Bluestein, 2012: The second verification of the origins of rotation in tornadoes experiment: VORTEX2. *Bull. Amer. Meteor. Soc.*, **93**, 1147–1170, <https://doi.org/10.1175/BAMS-D-11-00010.1>.
- , and Coauthors, 2021: The Flexible Array of Radars and Mesonets (FARM). *Bull. Amer. Meteor. Soc.*, **102**, E1499–E1525, <https://doi.org/10.1175/BAMS-D-20-0285.1>.
- Xu, X., M. Xue, and Y. Wang, 2015: The genesis of mesovortices within a real-data simulation of a bow echo system. *J. Atmos. Sci.*, **72**, 1963–1986, <https://doi.org/10.1175/JAS-D-14-0209.1>.